Ore Geology Reviews 163 (2023) 105771

Contents lists available at ScienceDirect

Ore Geology Reviews

journal homepage: www.elsevier.com/locate/oregeorev

Age of Carlin-type gold mineralization in the Youjiang basin, South China: Constraint from hydrothermal zircon geochronology in the Badu dolerite-hosted gold deposit

Wei Gao [a], Lu Mei [a,b], Ruizhong Hu [a,b,*], Shanling Fu [a], Xiaoyan Jiang [a], Jianwen Ma [c], Qiang Zhao [c]

[a] State Key Laboratory of Ore Deposit Geochemistry, Institute of Geochemistry, Chinese Academy of Sciences, Guiyang 550081, China
[b] College of Earth and Planetary Sciences, University of Chinese Academy of Sciences, Beijing 100049, China
[c] Jinfeng Mining Company, Tianlin 533315, China

ARTICLE INFO

Keywords:
The Youjiang basin
Carlin-type gold deposits
Hydrothermal zircon
SIMS and LA-ICP-MS U–Pb dating

ABSTRACT

Selecting a robust chronometer is crucial to determine the primary mineralization age of the deposits that have witnessed multiple hydrothermal events. The Youjiang basin of South China hosts the world's second-largest Carlin-type gold province. However, the age of the Carlin-type gold mineralization remains highly debated, partly due to the presence of multiple hydrothermal events that may have disturbed the primary isotopic system with low durability. Hydrothermal zircon is a robust chronometer that can survive multiple hydrothermal events. To this end, in this study, we report *in-situ* secondary ion mass spectrometry (SIMS) and laser ablation inductively coupled plasma-mass spectrometry (LA-ICP-MS) U–Pb dating results of hydrothermal zircon identified in carbonate–sericite–sulfide–altered dolerite from the Badu Carlin-type gold deposit to constrain the timing of gold mineralization.

The hydrothermal zircons exhibit subhedral to anhedral morphologies, sector cathodoluminescence zonings, and contain gold-related mineral assemblages of arsenian pyrite, quartz, sericite, and carbonate. Primary two-phase fluid inclusions also commonly occur in the hydrothermal zircons. Compositionally, these zircons feature relatively flat light rare-earth element (REE) patterns, high La contents, low $(Sm/La)_N$ values, and small Eu and Ce anomalies, which are different from the magmatic counterparts of the Badu pluton but consistent with those of hydrothermal zircons reported worldwide. These features indicate that the hydrothermal zircons are probably paragenetically associated with the gold mineralization. Consequently, the U–Pb ages of ca. 140 Ma of these zircons, which are much younger than those of the magmatic zircon in the fresh dolerite, can represent the timing of primary gold mineralization of Badu. Our new data suggests that there truly was an episode of gold mineralization during the Early Cretaceous in the Youjiang basin, which may have been driven by large-scale lithospheric extension in the interior of South China. This study demonstrates that hydrothermal zircon could be a robust clock for investigating the timing of magmatic rock-hosted Carlin-type gold deposits.

1. Introduction

Understanding the geological triggers driving the concentration of metallic elements (e.g., Au) to economic levels is the focus of ore genesis studies. This achievement largely relies on accurate and precise age constraints on such metal enrichment events. For example, benefiting from precise dating on hydrothermal apatite and wolframite, genesis of the well-known Woxi Au–Sb–W deposit, South China, has been linked to the Late Jurassic–Early Cretaceous extension related to Izanagi plate rollback (Li et al., 2023). However, for deposits that have witnessed multiple or protracted hydrothermal events, mineral chronometers starting during mineralization process may be disturbed or completely reset. Consequently, the primary mineralization age could be erased by younger hydrothermal activities (Li et al., 2021a, 2021b; Su et al., 2021a, 2023). To better date the primary mineralization, choosing a robust chronometer that can sturdily survive multiple hydrothermal events is necessary (Li et al., 2021a).

The Youjiang basin, located at the southwestern margin of South

* Corresponding author.
E-mail address: huruizhong@vip.gyig.ac.cn (R. Hu).

https://doi.org/10.1016/j.oregeorev.2023.105771
Received 29 May 2023; Received in revised form 4 November 2023; Accepted 5 November 2023
Available online 10 November 2023

China, is the world's second-largest Carlin-type gold province after Nevada, USA, with proven gold reserves of approximately 1000 t (Hu et al., 2020). Although the Carlin-type deposits in the basin have been the subject of many studies (summarized in Hu et al., 2017; Su et al., 2018), the absolute timing of gold mineralization relative to tectonic events is a topic of considerable debate, which hampers deeper understanding of the ore genesis. A wide range of techniques have been used to date these deposits, and ages ranging from 267 Ma to 60 Ma were initially obtained (Hu et al., 2017, and references therein). The highly variable ages raise the concern which age could truly represent the timing of gold mineralization. The recently reported isotopic ages (e.g., sulfide Re–Os, sericite Ar–Ar, and calcite Sm–Nd ages) are concentrated in two peaks, ca. 230–200 Ma and 160–130 Ma, indicating that two episodes of Carlin-type gold mineralization may exist in the Youjiang basin (Hu et al., 2017; Su et al., 2018). An alternative explanation is that the former age represents the primary gold mineralization event and the latter records only post-ore hydrothermal superposition that may have reset the primary chronometers (Ge et al., 2021; Li et al., 2022a; Hu et al., 2022; Wang et al., 2023). *In-situ* U–Pb dating results of hydrothermal calcite are also suggestive of multiple fluid infiltrations in the Youjiang Carlin-type deposits during the middle–Late Triassic to Late Cretaceous (Jin et al., 2021; Ge et al., 2022). This has further led to debate about whether the isotopically younger 160–130 Ma dates represent discrete Au mineralization event or post-ore reworking. Thus, a robust chronometer that can survive multiple hydrothermal events is needed.

Zircon is generally the most ideal and robust chronometer for U–Pb dating in various geological processes (Lee et al., 1997; Cherniak and Watson, 2003), because of its affinity for U and Th, negligible amount of initial Pb, and high durability and closure temperature (>800 ℃; Cherniak, 2010; Kooijman et al., 2011). Magmatic zircon U–Pb dating, in combination with hydrothermal molybdenite Re–Os age, have been applied widely to constrain the timing and duration of magmatic-hydrothermal mineralization systems, such as porphyry Cu–Mo–Au deposits (Chiaradia et al., 2013, 2014; Li et al., 2017, 2018). Additionally, an increasing number of cases suggests that zircon can crystallize directly from hydrothermal fluids with temperatures ranging from 600 °C at the magmatic-to-hydrothermal transition to 250 °C in mesothermal ore-forming systems (Hoskin, 2005; Pelleter et al., 2007; Schaltegger, 2007). In comparison to many hydrothermal minerals with isotopic systems susceptible to disturbance by subsequent processes, the hydrothermal zircon U–Pb system has been suggested to survive multi-stage hydrothermal events, even if the host rocks experienced intensive modification (Zhao et al., 2017; Li et al., 2021a; Su et al., 2021b). Therefore, when confidently identified, hydrothermal zircon can be used to robustly date primary fluid-infiltration or water/rock interaction events. To far, hydrothermal zircon has been successfully employed to constrain the mineralization ages of VMS deposits (Yeats et al., 1996; Nesbitt et al., 1999; Zhu et al., 2017), epithermal deposits (Lawrie et al., 2007; Zhou et al., 2012), orogenic or lode gold deposits (Claoué-Long et al., 1990; Kerrich and King, 1993; McNaughton et al., 2005; Pelleter et al., 2007; Bao et al., 2014; Käpyaho et al., 2017), iron oxide–copper–gold deposits (Valley et al.,2009; Zhao et al., 2017; Li et al., 2018), tungsten–tin deposits (Hoskin, 2005; Pettke et al., 2005; Schaltegger et al., 2005; Wang et al., 2016; Lamarao et al., 2018), skarn Fe deposits (Deng et al., 2015), REE deposits (Li et al., 2018, 2021a), and banded iron formations (Li et al., 2019). However, hydrothermal zircon has rarely been reported in low-temperature Carlin-type gold deposits, and whether the U–Pb chronometer of hydrothermal zircon can be used to date Carlin-type gold deposits is unknown.

In this study, we report the recognition of hydrothermal zircons from the Badu dolerite-hosted Carlin-type gold deposit in the Youjiang basin. Secondary ion mass spectrometry (SIMS) and laser ablation inductively coupled plasma-mass spectrometry (LA-ICP-MS) dating on these hydrothermal zircons was then conducted to uncover the Early Cretaceous Carlin-type gold mineralization in the Youjiang basin.

2. Regional geology

South China is composed of the Yangtze and Cathaysia Blocks, which were amalgamated along the Jiangshao Suture in the early Neoproterozoic (Fig. 1**a;** Zhao et al., 2011). The Youjiang basin is situated on the southwestern margin of the Yangtze Block, and is separated from the Indochina Block by the Song Ma Suture. It is a diamond-shaped basin with boundaries defined by four regional basement-penetrating faults, including the Mile–Shizong Fault to the northwest, the Ziyun–Du'an Fault to the northeast, the Pingxiang–Nanning Fault to the southeast, and the Red River Fault to the southwest (Fig. 1**b**).

The Youjiang basin experienced three stages of tectonic evolution (Yan et al., 2006; Du et al., 2009, 2013; Yang et al., 2012; Qiu et al., 2016): (1) rifted basin developed at the passive continental margin of South China during the early Devonian to early Permian (Du et al., 2009, 2013), (2) back-arc basin related to subduction of the Paleo-Tethys oceanic crust beneath South China during the middle-early Permian (Du et al., 2013), or subduction of the Paleo-Pacific plate beneath the Eurasian plate during the middle Permian (Li and Li, 2007), and (3) foreland basin due to closure of the Paleo-Tethys and the subsequent collision between the South China and the Indochina Blocks during the Middle-Late Triassic (Yan et al., 2006; Qiu et al., 2016). The collision formed a series of NW-trending folds and related faults that propagated NNE-ward through time (Qiu et al., 2016; Yang et al., 2021). During the Middle Jurassic, westward subduction of the Paleo-Pacific plate beneath South China formed NE-trending top-to-the-NW thrusting and fault-propagation folding, which superposed on the Triassic NWW-trending structures in the Youjiang basin (Qiu et al., 2016; Yang et al., 2021; Wang et al., 2022). Finally, these Mesozoic structures are crosscut by Cenozoic NE-SW-trending extensional normal faults (Qiu et al., 2016; Wang et al., 2022).

The Youjiang basin is covered by over 7000-m-thick marine sedimentary sequences that have been subjected to very low-grade burial metamorphism (Zhuang, 1995; Suo et al., 1998). The Triassic sedimentary rocks in the basin display two different sequences, separated by the Poping thrust fault, shallow-water carbonate platforms in the northwestern part of the basin and deep-water slope/basin calcareous sandstone, siltstone, and shale in the southeastern part, respectively (Fig. 1**b**, Du et al., 2013). Magmatic rocks in the basin are dominated by ca. 260 Ma Emeishan' plume-related dolerite and basalt mainly exposed in northwestern and southern parts of the basin (Zhou et al., 2006; Fan et al., 2008). Some dolerite dykes with ages of ca. 230–200 Ma, which were interpreted to form in a post-collisional setting, have been reported in the Funing-Napo region in southern margin of the basin (Pi et al., 2016; Jiang et al., 2017). Recently, a few Mg-high andesite with ages of ca. 160 Ma (Gan et al., 2020) and pegmatite dykes with ages of 145–140 Ma (Li et al., 2013a) were identified in the southwestern and southern margins of the basin, respectively. Additionally, some ultramafic and felsic dykes with ages of ca. 100–80 Ma are distributed in northwestern and southwestern parts of the basin, respectively (Liu et al., 2010a; Zhu et al., 2017). Petrogenesis of these Late Jurassic and Cretaceous magmatic rocks suggests an extensional setting of the Youjiang basin during this period (Liu et al., 2010a; Gan et al., 2020).

Carlin-type gold deposits in the Youjiang basin were firstly recognized (named Banqi deposit) in the early 1980 s. Recently, more than 200 Carlin-type gold deposits or occurrences, with estimated gold reserves of approximately 1000 t, have been reported in the basin (Hu et al., 2020). These deposits were clustered along the NW- and NE-trending regional faults. Gold mineralization is jointly controlled by lithologies and structures, and occurs as hydrothermal replacement orebodies preferentially hosted by the Late Permian bioclastic limestone interbedded with calcareous siltstone (e.g., the largest Shuiyindong deposit) and the Middle Triassic siltstone and mudstone (e.g., the second largest Jinfeng deposit; Su et al., 2018; Xie et al., 2018). Additionally, some unique gold deposits occurring in altered dolerite (e.g., Badu) or basalt (e.g., Jiadi) have recently been explored and mined (Gao et al.,

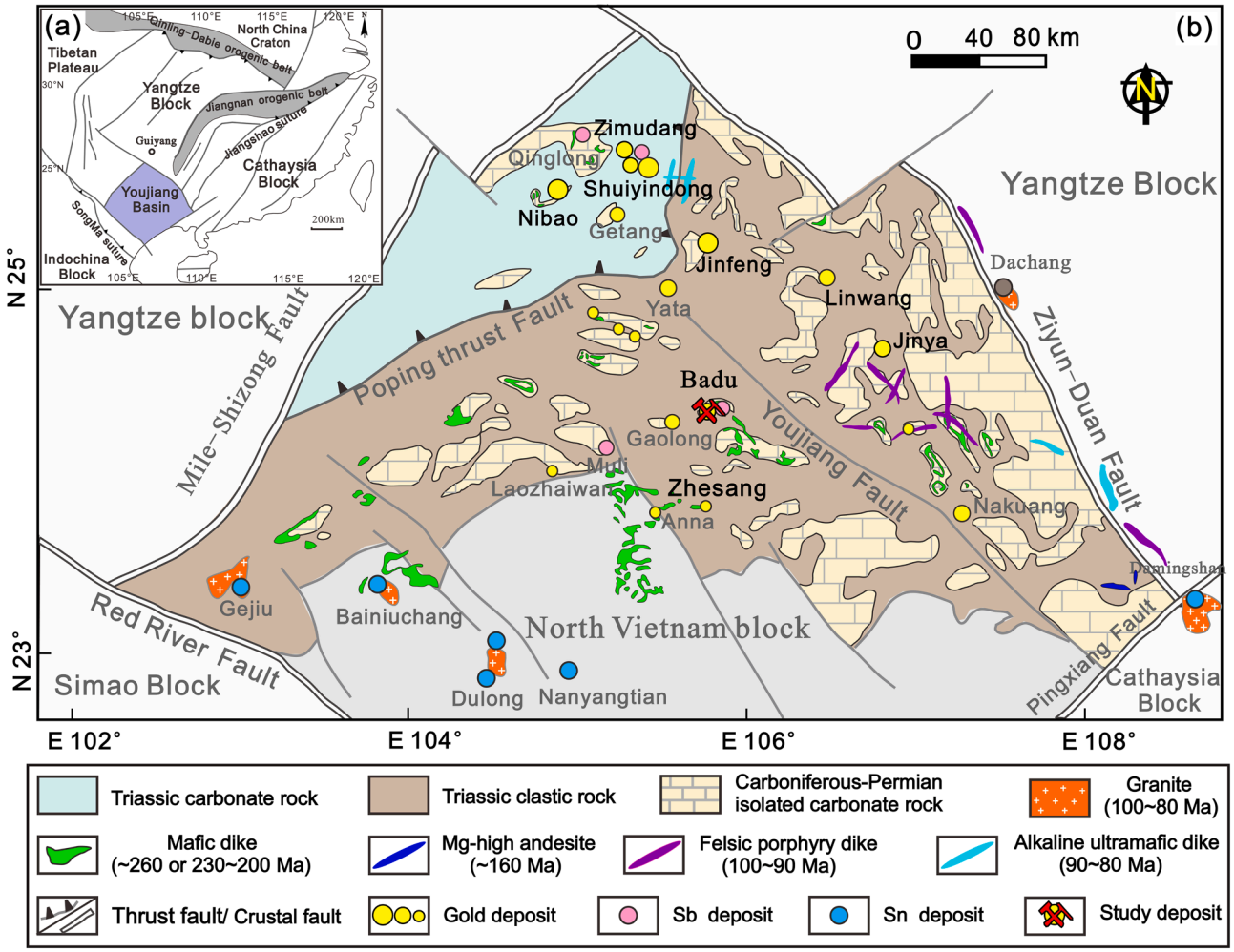

Fig. 1. (a) A simplified tectonic map of South China showing the location of the Youjiang basin. (b) A geologic map of the Youjiang basin showing the distribution of Carlin-type gold deposits and the Badu deposit (modified from Gao et al., 2021).

2021; Li et al., 2021). Integrating data suggest that these deposits share comparable characteristics with those of Carlin-type gold deposits in the Nevada, USA (Hu et al., 2002, 2017; Su et al., 2009, 2018; Xie et al., 2018; Wang and Groves, 2018; Gao et al., 2021), which mainly include: (1) signature ore elements of Au, As, Cu, Sb, Hg, and Tl, (2) 'invisible' gold of ionically-bound Au^{1+} and/or nanoparticles in disseminated arsenian pyrite or arsenopyrite, (3) wall-rock alteration of decarbonation, silicification, argillization, and sulfidation, (4) late ore-stage stibnite, realgar, orpiment, and calcite occurring as open space-fillings, (5) low-temperature (180–250 °C), low-salinity (<5 wt% NaCl equiv), CO_2-rich (6–75 mol %) and reduced fluids.

3. Deposit geology

The Badu deposit is located at the southern part of the Youjiang basin. Recent exploration showed that the deposit has an estimated gold reserve of 35 t (1.13 Moz) grading at 2 g/t (0.07 oz/t) (Jinfeng Mining Co., 2018, unpub. report). The detailed geology has been described by Gao et al. (2021).

The deposit is located on the western flank of the arc-shaped Badu anticline with a northward arcuate axis. The Badu anticline (Fig. 2), which has a Devonian core and Carbonaceous-to-Triassic limbs, experienced multiple tectonic superimpositions and was finally shaped by Indosinian deformation related to the formation of the Youjiang fold-and-thrust belt during the Middle-Late Triassic (Qiu et al., 2016; Yang et al., 2021). Series of *syn*-deformational faults, including NE-trending F_2, F_3, and F_4 faults and NW-trending F_1 and F_5 faults, crosscut the anticline. The NE-trending faults are dislocated dextrally by the NW-trending faults (Fig. 2**a**).

Within the ore district, the exposed strata mainly include marine sedimentary rocks of the lower Devonian Yujiang Formation, upper Devonian Liujiang Formation, Carboniferous, lower-middle Permian Sidazhai Formation, upper Permian Linghao Formation, lower Triassic Shipao Formation, and Middle Triassic Baifeng Formation (Fig. 2**a**). Numerous dolerite dykes intruded into the Devonian to Permian strata along NE- and NW-trending faults. The sedimentary rocks were slightly metamorphosed at the contacts. Early 1:50,000-scale geologic mapping divided the dolerites into three stages (BGMRGX, 1992). Recent dating efforts suggest multiple episodes of emplacement (Qiu et al., 2018; Xia et al., 2019; Gao et al., 2021).

The deposit contains seven major orebodies (numbered I to VII), which occur as veins and lenticulars in shape and are mainly controlled by NE-trending secondary faults (e.g., F_3 and F_4; Fig. 2**a**). The No. I and II orebodies are hosted within mudstone, siltstone, and sandstone of the lower Devonian Yujiang Formation. The No. III to VII orebodies occur within fractured dolerite with intense hydrothermal alteration, or along fault zones between dolerite and sedimentary strata (Fig. 2**b**). Field observations reveal that the gold mineralization is temporally later than the dolerite (Fig. 3**a**). Each orebody comprises sets of parallel veins with lengths between 10 and 500 m, widths from 2 to 70 m, and vertical distances below the surface of approximately 200 m.

The fresh dolerite has greyish green color and is mainly composed of

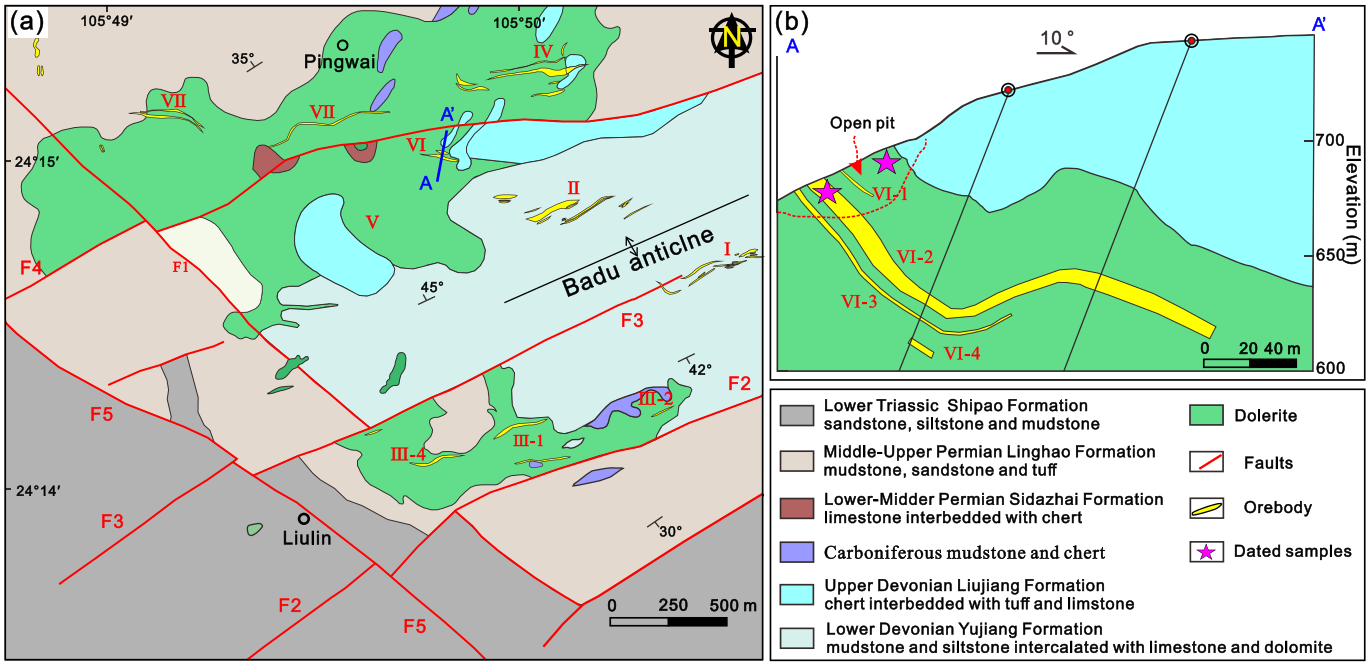

Fig. 2. (a) Schematic geologic map of the Badu deposit. (b) Geologic cross section of the dolerite-hosted No. VI orebody shown as lines a–a' in a (modified from Gao et al., 2021).

clinopyroxene (~45 vol%) and plagioclase (~50 vol%)with typical porphyritic texture (Fig. 3**b, c**). Minor ilmenite and titanite (~5 vol%) as well as trace apatite (<1 vol%) occur as accessory minerals displaying equilibrium textures with clinopyroxene and plagioclase. The mineralized dolerite has pale color because of strong hydrothermal bleaching and is characterized by abundant disseminated pyrite and arsenopyrite (~10 to 30 vol%, Fig. 3**d**). Hydrothermal alterations related to gold mineralization include mainly carbonation, sericitization, and sulfidation (Fig. 3**e**). Macro- and microtextural relationships suggest four principal stages of alteration and mineralization: (1) Magmatic pyroxene and plagioclase were firstly replaced by ankerite and sericite, which mimics the poikilophitic texture of the clinopyroxene and plagioclase (Fig. 3**f**). Magmatic ilmenite and titanite were replaced by pseudomorphic intergrowths of rutile and ankerite (Gao et al., 2021); (2) The early formed ankerite was gradually replaced by pyrite and arsenopyrite (Fig. 3**g**). Ankerite, sericite, and rutile were enclosed in pyrite grains during sulfidation, forming inclusion-rich anhedral pyrite cores, which are surrounded by an inclusion-free outer pyrite rim (Fig. 3**h**). Such textures suggest that the pyrite cores formed during or after formation of ankerite and sericite. Nano-SIMS and LA-ICP-MS analyses suggest that both the pyrite cores and rims contain variable amounts of 'invisible gold' in their lattice (Gao et al., 2022; Wei et al., 2022), clarifying that they represent the main period of gold deposition. Trace hydrothermal monazite, zircon, and apatite, all which intergrown with gold-bearing pyrite, have also formed during this stage. (3) Ore pyrite grains were brittlely fractured, forming a series of microfractures that were filled by some chalcopyrite, tetrahedrite, tennantite, and sphalerite (Fig. 3**i**). Because these sulfosalt and base mental sulfides are confined to the mineralized dolerite and closely follows the formation of ore pyrite, they may have precipitated from an evolving ore-forming fluids as a result of fluids consumption and cooling and, therefore, formed during the transition from the ore-stage to late-Sb–Hg mineralization-stage (Gao et al., 2021). (4) Multiple quartz-ankerite veins of varying widths, together with stibnite, realgar, and cinnabar open space fillings, constitute the paragenetically late minerals crosscutting all previous stages. Finally, the wanning of hydrothermal systems is represented by the formation of some calcite veins (Fig. 4).

Gao et al. (2021) have systemically compared the characteristics between the Badu and other sedimentary rock-hosted Carlin-type gold deposits in the Youjiang basin, e.g., the Shuiyindong and Jinfeng, and concluded that the Badu is simply a dolerite-hosted equivalent of the other Carlin-type gold deposits. Some key comparable features include: (1) pre-ore reactive Fe-bearing minerals (e.g., clinopyroxene, titanite, and ilmenite) as chemical requirement for gold mineralization, resembling Fe-bearing carbonate in -sedimentary rock-hosted Carlin-type deposits (Stenger et al., 1998); (2) Fe-bearing minerals dissolution and sulfidation of the released Fe during hydrothermal replacement, forming gold-bearing arsenian pyrite, which is reminiscent of carbonate dissolution and sulfidation in sedimentary rock-hosted Carlin-type deposits (Su et al., 2009); (3) typical ore element associations of Au, As, Cu, Sb, and Hg, with gold occurring as 'invisible' forms in lattice of arsenian pyrite (Gao et al., 2022); (4) similar mineral paragenesis comprising ore-stage disseminated arsenian pyrite and late ore- stage fractures or open space-fillings stibnite, realgar, orpiment, and calcite; (5) fluid inclusions with low temperatures of 201° to 301 °C (with a mode of 245 °C) and low salinities (0.02 ~ 3.52 wt% NaCl equiv; Dong, 2017).

4. Sampling and analytical methods

Two zircon-bearing mineralized dolerite samples were collected from the open pit of the most representative No. VI orebody in the Badu deposit in 2018 and 2020, respectively. The samples display strong carbonation, sericitization, and sulfidation alterations, and are characterized by dense disseminations of gold-bearing pyrite and subordinate arsenopyrite. Hydrothermal zircons in the mineralized dolerite were firstly identified and dated using LA-ICP-MS in 2018. A duplicate sample was collected again in 2020, and the same hydrothermal zircons were identified and then dated using SIMS, reconfirming the true occurrence of hydrothermal zircons. Each mineralized sample weighed at least 60 kg.

Zircon grains were separated from the samples by crushing, sieving, and magnetic and heavy liquid methods and then handpicked under a binocular microscope. These zircon grains, together with standards, were mounted on epoxy resin disks and polished to expose the half of grains for subsequent petrographic observation and analysis. The morphology and internal structure of the zircons were characterized by

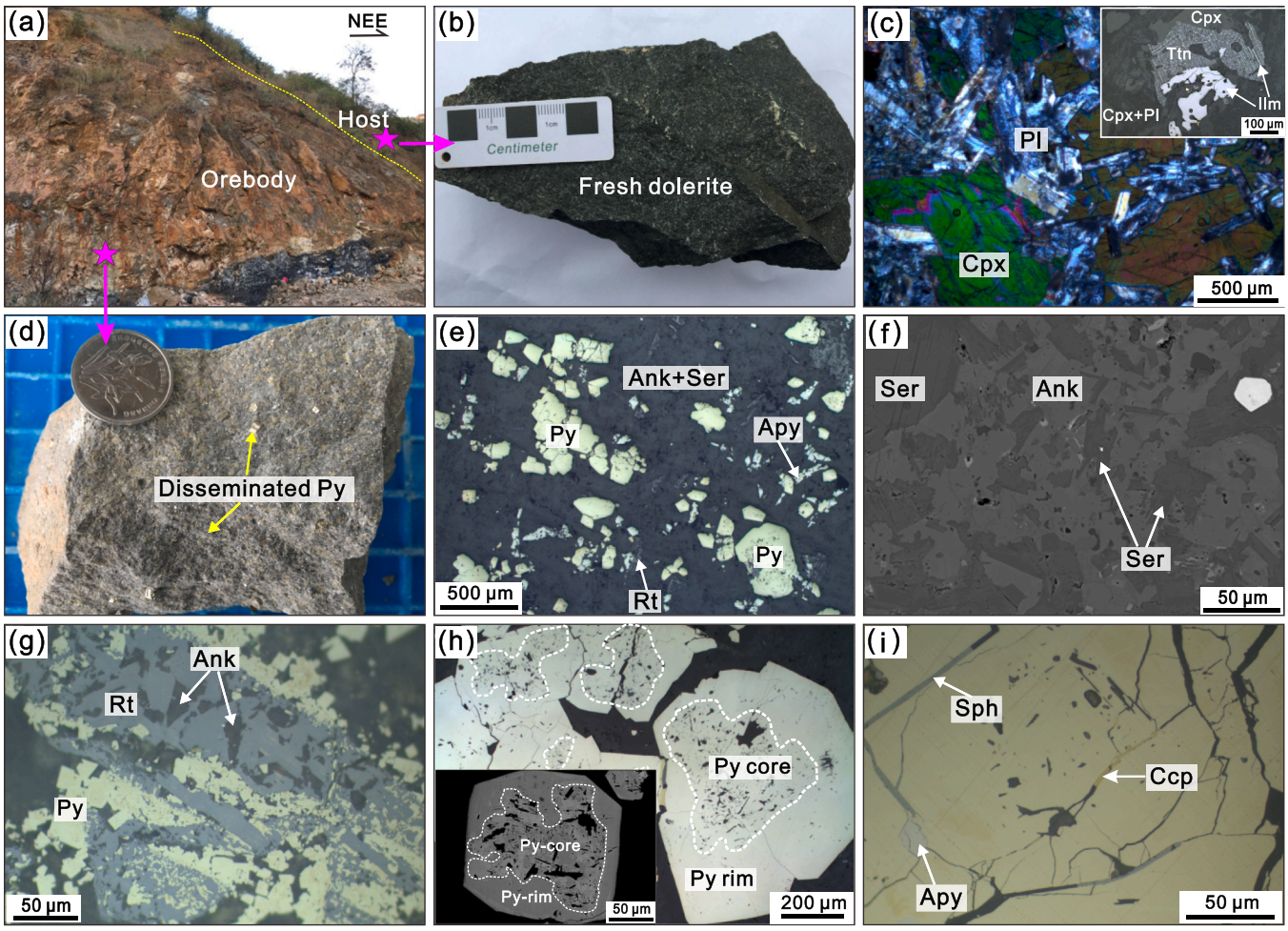

Fig. 3. (a) A field photo of No. VI orebody showing the locations of the zircon-bearing samples from the fresh and mineralized dolerite, respectively. (b, c) Photograph of hand specimen and photomicrograph for the zircon-bearing fresh dolerite. (d, e–g) Photograph of hand specimen and photomicrograph for the zircon-bearing mineralized dolerite. (h) Photomicrograph of typical gold-bearing pyrite showing inclusion- and As-rich core and clean rim. (i) Photomicrograph of late-stage sulfide infillings along the fractures of gold-bearing pyrite. Abbreviations: Cpx = clinopyroxene, Pl = plagioclase, Ttn = titanite, Ilm = ilmenite, Py = pyrite, Ank = ankerite, Ser = sericite, Rt = rutile, Apy = arsenopyrite, Sph = sphalerite, Ccp = chalcopyrite.

transmitted and reflected light, scanning electron microscopy with a backscattered electron (SEM-BSE), and cathodoluminescence (CL). Then, the carbon coatings in mounts were clearly erased before LA-ICP-MS and SIMS analysis. Portions of the grains without visible inclusions or cracks were chosen as analytical locations. For comparison, magmatic zircon grains from the fresh dolerite adjacent to the No. VI orebody, which were dated at 212.2 ± 2.3 Ma (2σ, MSWD = 1.2) by Gao et al. (2021), were also characterized and analyzed to obtain trace element compositions.

4.1. SIMS zircon dating

In-situ SIMS zircon dating was conducted using a Cameca IMS-1280HR SIMS at the Institute of Geology and Geophysics, Chinese Academy of Sciences in Beijing, China. The mounts were vacuum-coated with high-purity gold prior to SIMS dating. The detailed instrument parameters and analytical methods can be found in Li et al. (2009). A brief description is summarized here. An O^{2-} primary ion beam was accelerated at 13 kV. The ellipsoidal spots are about 10 × 15 μm in diameter. Positive secondary ion was extracted with a 10 kV potential. The Zr_2O^+ signal was used as a reference peak for centering the secondary ion beam, energy, and mass adjustment. A mass resolution of ca. 5400 (at 10 % peak height) was used to separate Pb^+ peaks from isobaric interferences. A single electron multiplier was utilized to measure the secondary ion intensity by peak jumping mode. Each measurement consists of 7 cycles and the total analytical time is ca. 15 min.

Pb/U calibration was performed relative to standard Plesovice ($^{206}Pb/^{238}U$ age = 337.1 ± 0.37 Ma, Sláma et al., 2008); U and Th concentrations were calibrated against zircon standard 91,500 (Th = 29 ppm, and U = 81 ppm, Wiedenbeck et al., 1995). A long-term uncertainty of 1.5 % (1 s RSD) for $^{206}Pb/^{238}U$ measurements of the standard zircons was propagated to the unknowns (Li et al., 2010), despite that the measured $^{206}Pb/^{238}U$ error in a specific session is generally ≤ 1 % (1 s RSD). Measured compositions were corrected for common Pb using non-radiogenic ^{204}Pb. Corrections are sufficiently small to be insensitive to the choice of common Pb composition, and an average of present-day crustal composition (Stacey and Kramers, 1975) is used for the common Pb assuming that the common Pb is largely surface contamination introduced during sample preparation. Data reduction was carried out using the Isoplot/Ex v. 3.0 program (Ludwig, 2003). Uncertainties on individual analyses in data tables are reported at 1σ level; Concordia U-Pb ages are quoted with 95 % confidence interval, except where noted otherwise. In order to monitor the external uncertainties of SIMS U-Pb zircon dating calibrated against Plesovice standard, an in-house zircon standard Qinghu was alternately analyzed as an unknown together with other unknown zircons. Twenty-two measurements on Qinghu zircon yield a Concordia age of 159.2 ± 2.2 Ma, which is identical within error with the recommended value of 159.5 ± 0.2 Ma (Li et al., 2013b).

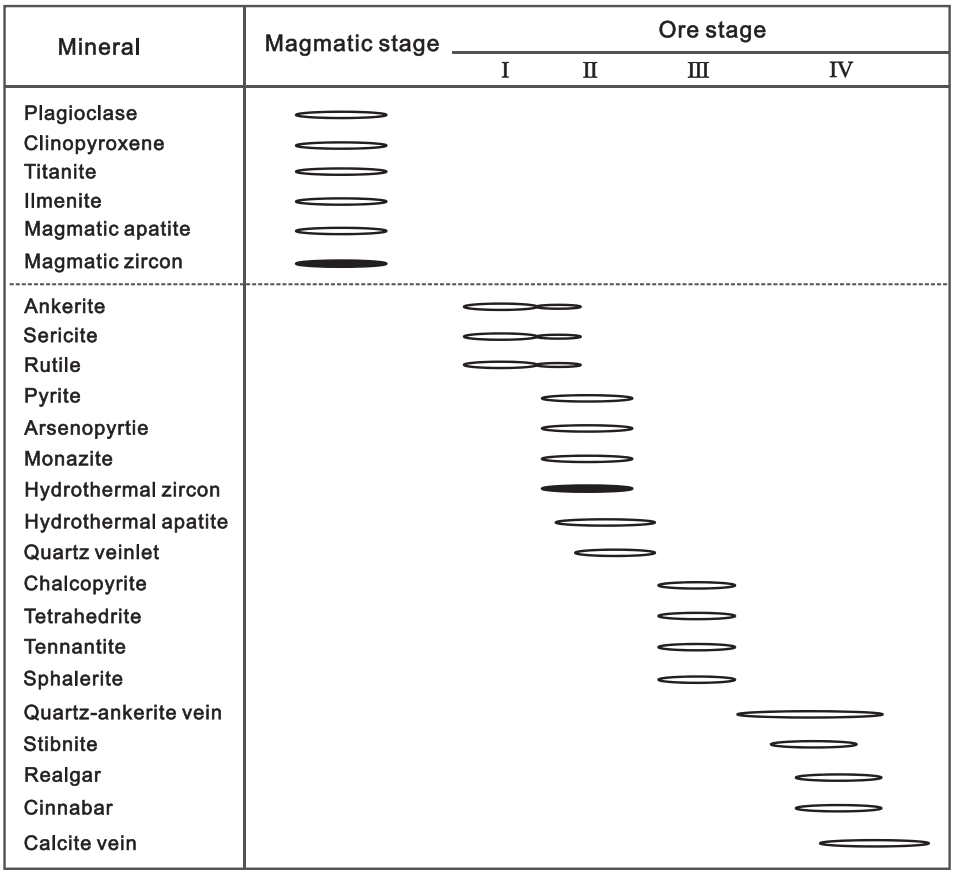

Fig. 4. Mineral paragenesis of the Badu dolerite rock-hosted gold deposits in the Youjiang basin.

4.2. LA-ICP-MS zircon dating and trace element analyses

The U-Th-Pb isotopies and trace element analysis were performed simultaneously on zircon, using an Agilent 7900 type inductively coupled plasma-mass spectrometry (ICP-MS) equipped with a GeolasPro 193 nm ArF excimer laser ablation (LA) system at the State Key Laboratory of Ore Deposit Geochemistry, IGCAS. The analytical procedures were similar to those described by Liu et al. (2008, 2010b). A laser repetition rate of 6 Hz, energy density of 3 J/cm^2, and spot size of 25 μm were used for analysis. The counting times of each spot analysis were approximately 20 s, 40 s, and 20 s for the background data acquisition, sample data acquisition, and wash-out, respectively. For dating, zircon standard 91500, whose U-Th-Pb isotopic ratios are from Wiedenbeck et al. (1995), was used as the external isotopic calibration and was analyzed twice every 8–10 analyses. For each analysis, the time-resolved signals were inspected to monitor the presence of inclusions or common Pb. Zircon standards Plešovice and Qinghu were used for quality control and obtained the consistent age of 338 ± 5.2 Ma (N = 5) and 159.6 ± 3.1 Ma (N = 5), respectively. Trace element concentrations of zircon were calibrated using glass standard NIST610 as the external standard and theoretical value of Si content in zircon as the internal standard. Data processing was carried out using the software ICPMSDataCal (Liu et al., 2008, 2010b). Age calculation was performed using the Isoplot/Ex v. 3.0 progarm (Ludwig, 2003).

5. Results

5.1. Zircon petrography

Zircon grains from the fresh dolerite were previously characterized by Gao et al. (2021). Here, we focus only on magmatic zircons with ages of ca. 210 Ma. The zircons have euhedral to subhedral shapes, lengths of 50 to 100 μm, and aspect ratios of 3:1. Under the CL images, they are dark gray and show relatively homogenous textures, with little or no zoning (Fig. 5**a**), consistent with typical magmatic zircon in mafic rocks (Corfu et al., 2003).

Zircon grains extracted from the mineralized dolerite with carbonate–sericite–sulfide alterations show three types of textures and CL images (Fig. 5**b**). Type 1 zircons have euhedral to subhedral margins and oscillatory CL zoning, and locally contain small cores. Type 2 zircons have dark CL images with faintly oscillatory or relatively homogeneous zonings. Type 3 zircons are subhedral to anhedral in shape and have irregular margins with diameters from 20 to 100 μm (Fig. 5**b**). They commonly display multi-facetted growth habit forms and exhibit irregular sector, patchy, and chaotic zoning in CL images (Fig. 5**b**). Some zircon grains contain hydrothermal mineral inclusions of arsenian pyrite intergrown with quartz, sericite, and ankerite (Fig. 5**c, d**). These minerals are consistent with the mineral paragenesis associated with gold mineralization. Rarely, small grains of native gold are enclosed within the zircon (Fig. 5**d**). Some zircons occur as 20–50-μm-thick rims overgrowing on magmatic zircon and is riddled with mineral inclusions of quartz, sericite, and ankerite (Fig. 5**e**). Some zircons have larger fractures with fillings of late ore-stage realgar or stibnite (Fig. 5**f**). Another striking feature in these zircons is the common presence of primary two-phase liquid fluid inclusions (Fig. 5**g, h**).

5.2. Zircon dating results

The SIMS and LA-ICP-MS zircon U–Pb dating results are provided in A ppendix Tables A1 and A2, respectively. For SIMS dating, twenty-three analyses were conducted on 23 zircon grains in a single analytical session. Among these, seven grains with oscillatory CL zoning or dark CL

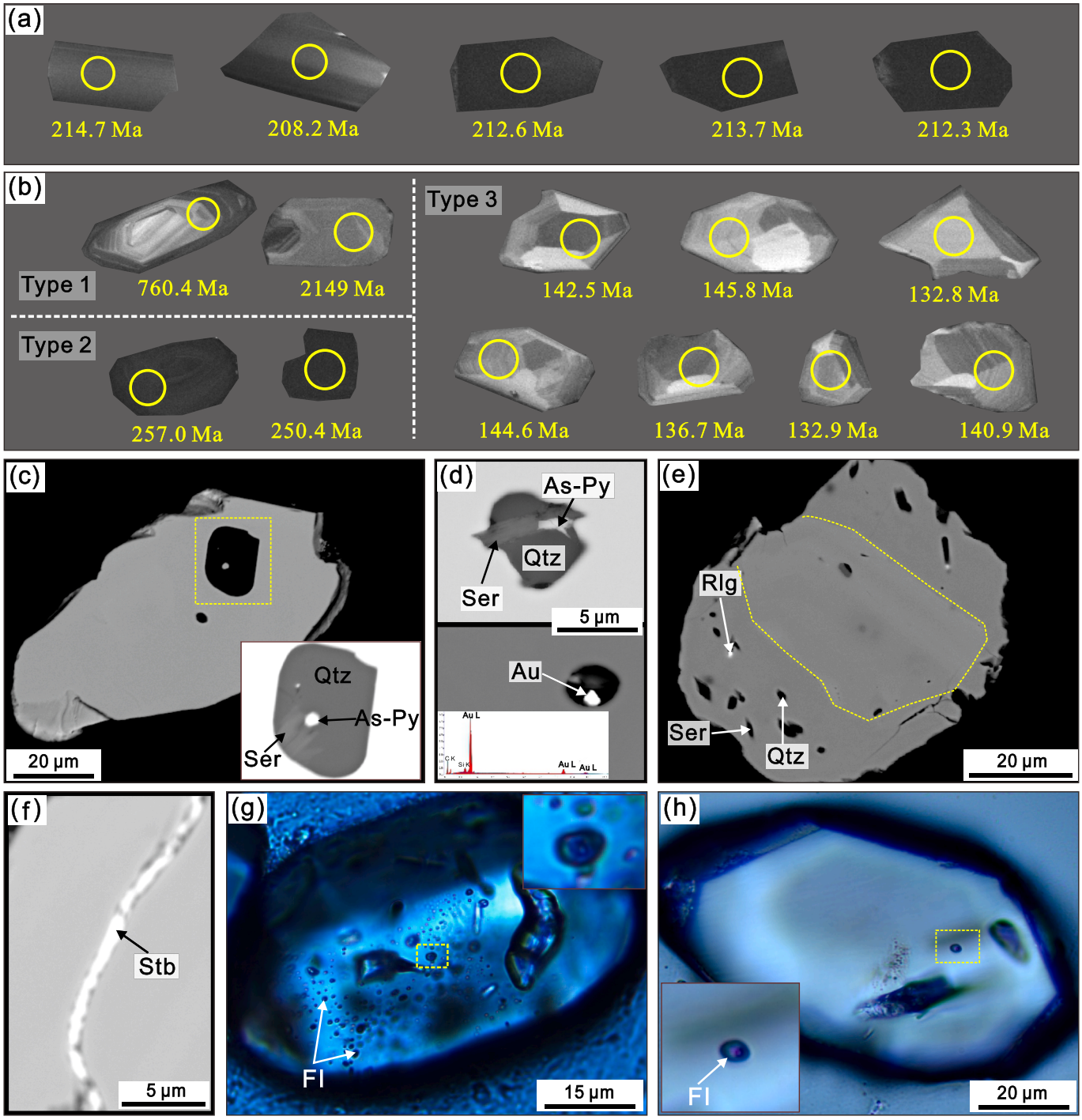

Fig. 5. Photomicrographs in CL images (a, b), backscattered electron images (c-f), and transmitted light (g, h) showing characteristics of zircon grains in the Badu deposit. (a) Magmatic zircon with homogeneous CL images from the fresh dolerite. (b) Inherited zircon with oscillatory CL zoning (type 1) and dark CL images (type 2), and hydrothermal zircon with sector or patchy zoning (type 3) from the mineralized dolerite. (c, d) Hydrothermal zircon grains containing gold-related mineral inclusions. (e) Hydrothermal zircon occurring as overgrowth with gold-related mineral inclusions. (f) Hydrothermal zircon crosscut by transgranular fracture with infilling of stibnite. (g, h) Hydrothermal zircon with primary two-phase fluid inclusions. Abbreviations: Qtz = quartz, Ser = sericite, As-Py = arsenian pyrite, Rlg = realgar, Stb = stibnite, FI = fluid inclusion.

images yield old $^{206}Pb/^{238}U$ ages from 250.4 ± 2.4 to 2149 ± 144.4 Ma (Fig. 5**b**). The remaining 16 grains with sector or patchy CL zoning have moderate U (104——937 ppm) and Th (87——972 ppm) contents, with Th/U ratios between 0.5 and 1.1. These zircon grains have $^{206}Pb/^{238}U$ ages ranging from 129.3 ± 2.4 to 145.8 ± 3.1 Ma, yielding an intercept age of 144.4 ± 5.9 Ma (2σ, MSWD = 0.72) in the $^{207}Pb/^{235}U$ vs $^{206}Pb/^{238}U$ diagram (Fig. 6**a**). Among these, three spots contain non-negligible amounts of common Pb, with f_{206} (the proportion of common Pb) values ranging from 6.2 % to 19.7 %. Thus, the popular ^{207}Pb-based common Pb correction was employed to subtract common Pb (Williams, 1998; Li et al., 2012), with the common Pb composition estimated using the terrestrial Pb isotope composition for the corresponding ages (Stacey and Kramers, 1975). In this study, the uncorrected $^{206}Pb/^{238}U$ and $^{207}Pb/^{206}Pb$ data points were plotted on a Tera-

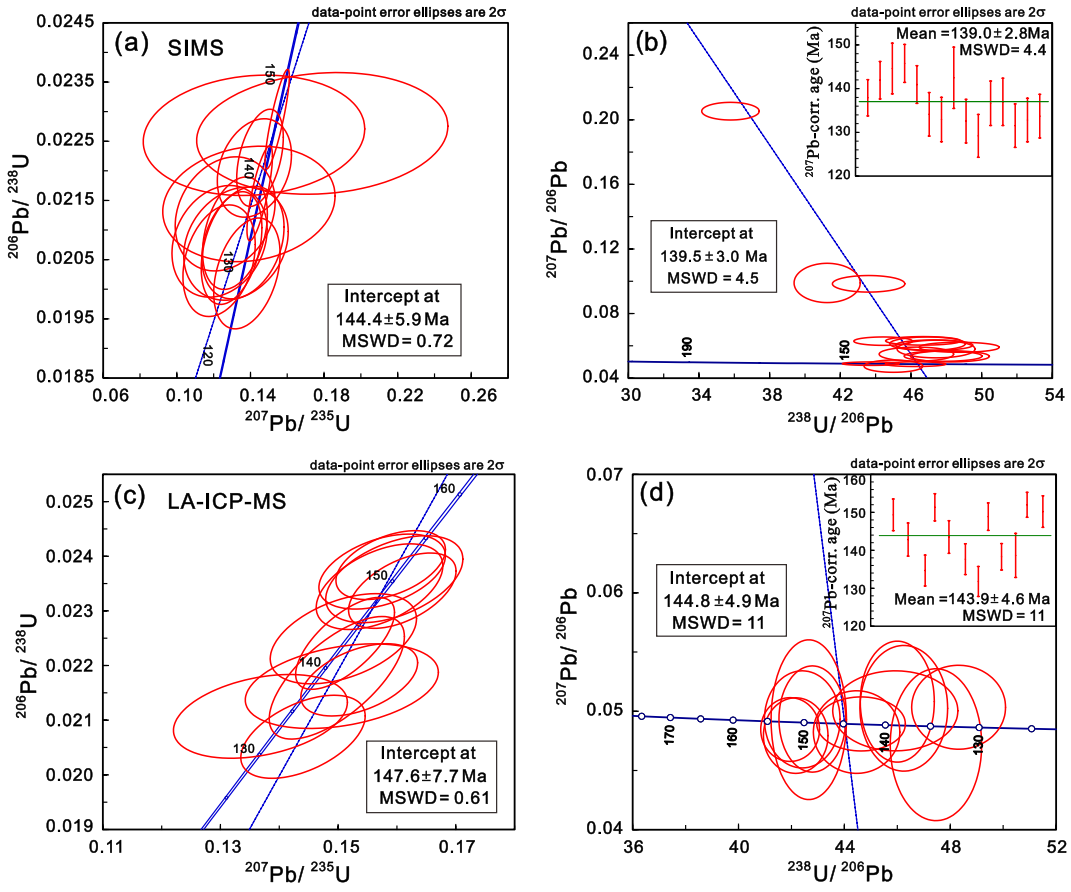

Fig. 6. Dating results of hydrothermal zircons in the Badu deposit. (a, b) Concordia diagram and Tera-Wasserburg U-Pb plot for hydrothermal zircon dated by SIMS. (c, d) Concordia diagram and Tera-Wasserburg U-Pb plot for hydrothermal zircon dated by LA-ICP-MS.

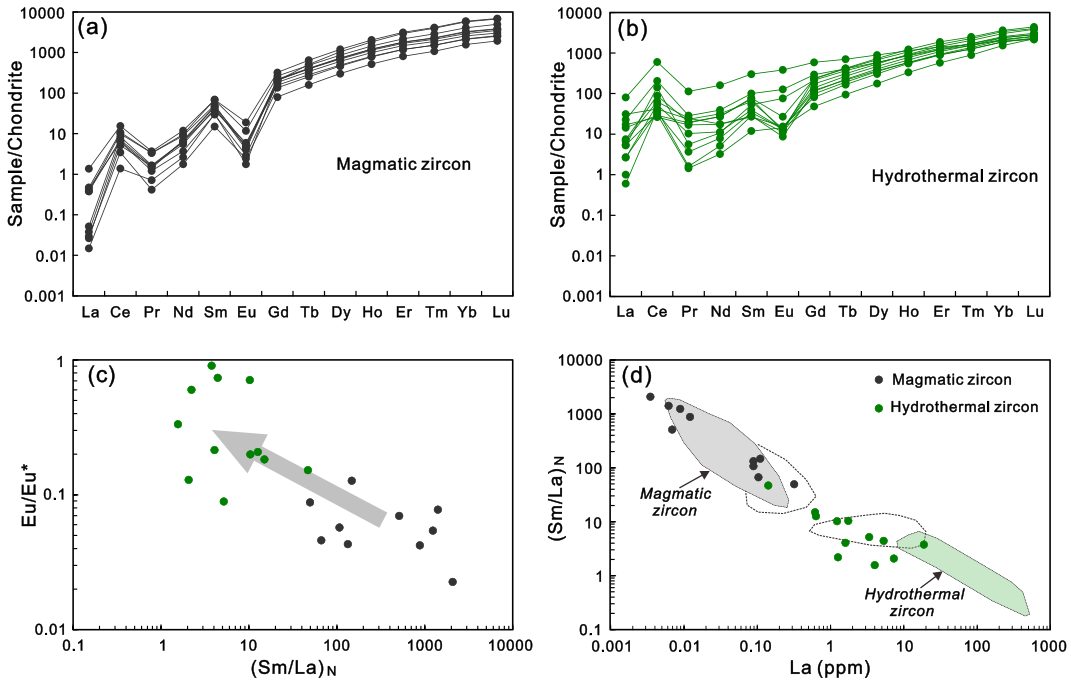

Fig. 7. (a, b) Chondrite-normalized REE patterns for magmatic zircon from the fresh dolerite and hydrothermal zircon from the mineralized dolerite in Badu, respectively. (c) Eu/Eu* vs. $(Sm/La)_N$ plot showing the decreased Eu anomalies from magmatic to hydrothermal zircon due to plagioclase breakdown. (d) $(Sm/La)_N$ vs. La discrimination diagram for magmatic zircon from hydrothermal zircon (Hoskin, 2005). Data of hydrothermal zircon from mineralized dolerite are plotted between the fields between magmatic and hydrothermal zircon, yet close enough that limited extension of the fields (dashed line), which is consistent with that of Hoskin. (2005).

Wasserburg diagram (Tera and Wasserburg, 1972; Fig. 6**b**), which defines a lower intercept age of 139.5 ± 3.0 Ma (2σ, MSWD = 4.5). Using an estimated $^{207}Pb/^{206}Pb_{common}$ value of 0.845 (age = 140 Ma) based on the terrestrial-Pb evolution model (Stacey and Kramers, 1975), a weighted average ^{207}Pb-corrected age of 139.0 ± 2.8 Ma (2σ, MSWD = 4.4) was calculated, representing the timing of zircon crystallization.

For LA-ICP-MS dating, eighteen analyses were conducted on 18 zircon grains. Among these, three analyses are excluded for concordance lower than 95 %. Two grains with oscillatory CL zoning or dark CL images yielded old $^{206}Pb/^{238}U$ ages of 2163 ± 30.5 Ma and 255.4 ± 3.2, respectively. The remaining 13 grains with sector or patchy CL zoning have moderate to high U (214——1484 ppm) and Th (133.2——1179 ppm) contents, with Th/U ratios of 0.4——1.5. They have $^{206}Pb/^{238}U$ ages from 130.2 ± 1.8 to 151.9 ± 1.6 Ma, yielding an intercept age of 147.6 ± 7.7 Ma (2σ, MSWD = 0.61) in the $^{207}Pb/^{235}U$ vs $^{206}Pb/^{238}U$ diagram (Fig. 6**c**). On the Tera-Wasserburg diagram (Fig. 6**d**), they define a lower intercept age of 144.8 ± 4.9 Ma (2σ, MSWD = 11), with average ^{207}Pb-corrected age of 143.9 ± 4.6 Ma (2σ, MSWD = 11).

5.3. Zircon trace element

The zircon trace element results are tabulated in A ppendix Table A3. Zircon grains with sector or patchy CL zoning from the mineralized dolerite contain total REE contents of 536 to 1656 ppm, with an average value of 1054 ppm, both which are slightly lower than the values of magmatic zircon (611–2340 ppm, average of 1350 ppm) from the fresh dolerite. In the chondrite-normalized REE diagram (McDonough and Sun, 1995; Fig. 7**a**), zircon grains from the fresh dolerite show steep positive slopes from La to Lu. They are enriched in heavy REEs (HREEs; 605–2316 ppm) but relatively depleted in light REEs (LREE; 5.4–26.7 ppm), with high HREE/LREE ratios (61–311) and $(Sm/La)_N$ values (49.5–2067). Moreover, they have evidently positive Ce (Ce/Ce* = 6.93–31.3) and markedly negative Eu (Eu/Eu* = 0.02–0.13) anomalies. In contrast, zircon grains with sector or patchy CL zoning from the mineralized dolerite display relatively flatter chondrite-normalized REE patterns (Fig. 7**b**), have much higher La (0.14–19.0 ppm) and LREE (24.6–541 ppm) contents, with lower HREE/LREE ratios (2.06–29.7) and $(Sm/La)_N$ values (1.56–15.0). They yielded positive Ce anomalies with Ce/Ce* = 1.54–39.1, comparable with those in magmatic zircons. However, their negative Eu anomalies (Eu/Eu* = 0.09–0.91) are highly variable and significantly lower than those of the magmatic zircons (Fig. 7**c**). In the La vs $(Sm/La)_N$ diagram, the zircon grains from the fresh and mineralized dolerite are plotted in the magmatic and hydrothermal fields, respectively (Fig. 7**d**).

6. Discussion

6.1. Hydrothermal origin of the zircon in the mineralized dolerite of Badu

The dolerite in the Badu district emplaced mainly into Devonian to Permian strata, indicating that the individual ages of any inherited zircons captured during emplacement (if present) should be older than Permian and scattered. However, zircon grains from the fresh and mineralized dolerites yielded two uniform and much younger age groups, ca. 210 Ma and ca. 140 Ma, respectively, suggesting that an inheritance origin of both types of zircons can be ruled out. The zircons with ages of ca. 210 Ma from the fresh dolerite display blocky, homogeneous, and dark-gray CL images with no zoning, exhibit chondrite-normalized REE patterns characterized by steeply positive slopes from La to Lu, and have large positive Ce anomalies and negative Eu-anomalies. All these features are consistent with those of typical igneous zircons from mafic rocks described worldwide (Corfu et al., 2003; Fan et al., 2008; Su et al., 2021b), suggesting that the zircons crystallized from dolerite magma and, therefore, that the Badu dolerite emplaced in the Late Triassic.

In contrast, the zircon grains with age of ca. 140 Ma from the mineralized dolerite exhibit textural and compositional characteristics that are strikingly distinct from those of the magmatic zircons, indicating that they may have a different origin. These zircons are characterized by anhedral morphologies and irregular sector or patchy CL zonings, which are similar to metamorphic or hydrothermal zircons reported worldwide (Pelleter et al., 2007; Chen et al., 2010, 2011; Deng et al., 2015; Li et al., 2018, 2021a, 2022b). Given that the sedimentary strata in the Youjiang basin have only experienced very low-grade metamorphism since the Mesozoic (Suo et al., 1998) and that magmatic minerals in the fresh dolerite of Badu have well-preserved primary textures with no metamorphic features, a metamorphic genesis of these zircons is also unlikely.

Alternatively, the zircon grains with age of ca. 140 Ma display several striking features, although the extremely low zircon concentrations made it difficult to observe them in thin sections in their textural context. Firstly, they occur only in mineralized dolerite with carbonate–sericite–sulfide alterations. Some of these zircons contain mineral inclusions of gold-bearing pyrite, quartz, ankerite, and sericite. These minerals are consistent with the ore-stage paragenesis associated with gold mineralization and appear to have been trapped as primary inclusions during zircon growth, with no evidence of later precipitation along fractures or pores. The presence of quartz inclusions further indicates a non-magmatic origin for these zircons, given that mafic magma is generally unsaturated with Si. Therefore, the primary quartz inclusions in the zircons are unlikely to crystalize from the magma and was then trapped in the zircon. Secondly, the zircon grains commonly contain primary two-phases fluid inclusions with characteristics similar to those hosted in the ore-stage quartz veinlets (Dong, 2017; Su et al., 2018), implying that they formed from hydrothermal fluids. Thirdly, some zircon grains show infillings of late ore-stage realgar or stibnite along transgranular fractures. These integrated petrographic evidences are widely regarded as being the most reliable arguments supporting a hydrothermal origin for zircon (Kerrich and King, 1993; Nesbitt et al., 1999; Pettke et al., 2005; Lawrie et al., 2007; Toscano et al., 2014). Accordingly, the zircons dated with age of ca. 140 Ma from the mineralized dolerite are of hydrothermal origin and their crystallization is likely related to gold mineralization, but earlier than late ore-stage Sb–Hg mineralization.

The compositions of these zircon grains are also supportive of their hydrothermal origin. Firstly, they have notably higher and variable La and Ce contents, resulting in relatively enriched LREEs and flatter chondrite-normalized REE patterns, a feature that does not accord with the pattern of magmatic zircons, but is in good agreement with the typical hydrothermal zircon patterns (Hoskin, 2005; Pettke et al., 2005; Pelleter et al., 2007; Schaltegger, 2007; Zhou et al., 2012; Ayers and Peters, 2018; Li et al., 2021a). Secondly, they display highly variable and much weaker negative Eu anomalies relative to those of magmatic zircons. This composition can be interpreted by the breakdown of magmatic plagioclase with positive Eu anomalies during the fluids–rock interaction related to gold mineralization. Thirdly, on the $(Sm/La)_N$ vs. La diagram, which has been demonstrated to be effective at discriminating hydrothermal zircon from its magmatic counterpart (Hoskin, 2005; Zhou et al., 2012; Yang et al., 2014; Li et al., 2021a), almost all zircon grains plotted within or near the hydrothermal zircon field described by Hoskin (2005).

6.2. Early Cretaceous Carlin-type gold mineralization in the Youjiang basin

Although a wide range of methods have been utilized for various minerals (Fig. 8**a**), the timing of the Carlin-type gold deposits in the Youjiang basin remain highly debated. Recently, bulk analyses on separates of sulfides (Re–Os or Rb–Sr, Liu et al., 2014; Chen et al., 2015; Dong, 2017; Ge et al., 2021), sericite or illite (^{40}Ar–^{39}Ar, Chen et al., 2009; Pi et al., 2016; Dong, 2017), and calcite (Sm–Nd; Su et al., 2009; Jin, 2017; Wang et al., 2021) suggested two episodes of Carlin-type gold

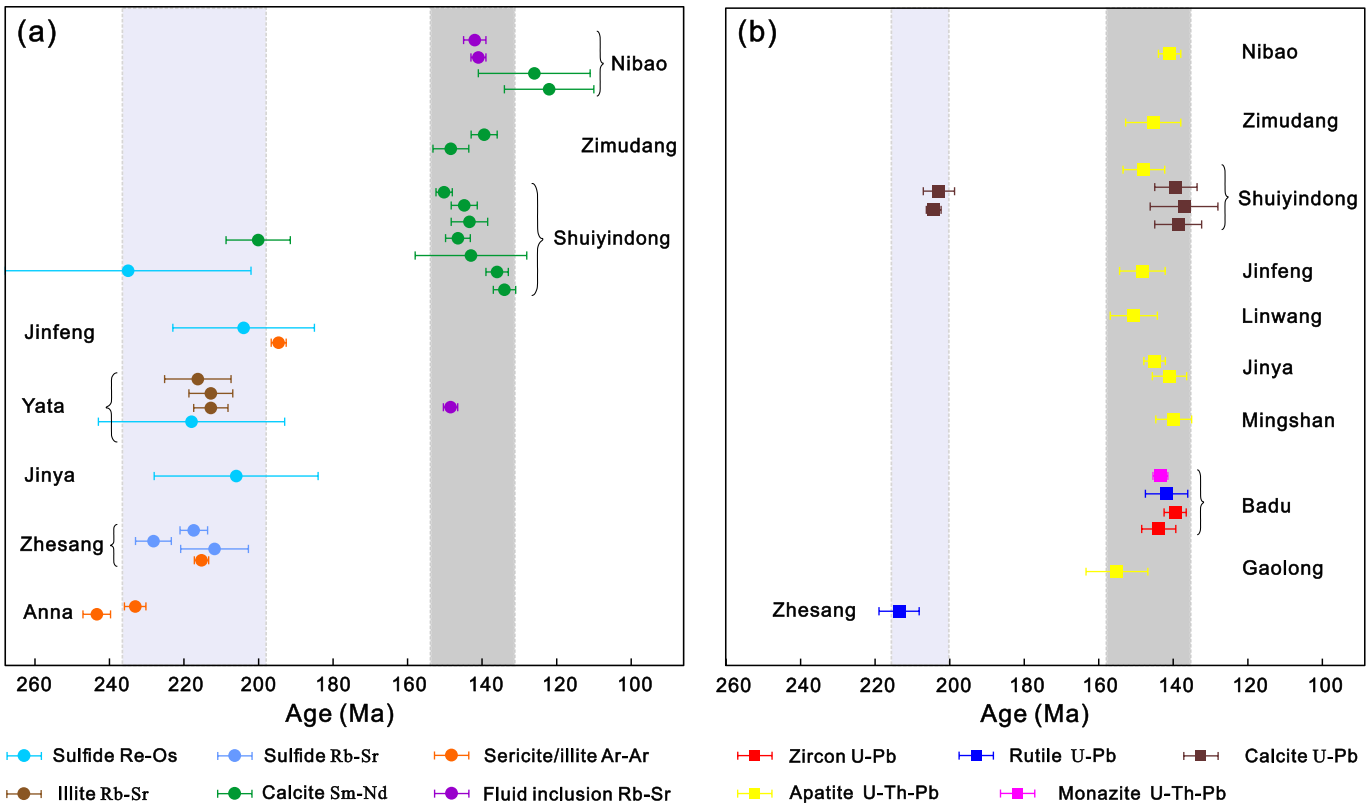

Fig. 8. Summary of dissolution-based (a) and in-situ (b) dating results of the Carlin-type gold deposits in the Youjiang basin. The data sources of the sulfide Re–Os or Rb–Sr ages are from Liu et al. (2014), Chen et al. (2015), Dong. (2017), and Ge et al. (2021); for the sericite or illite Ar–Ar ages are from Chen et al. (2009), Pi et al. (2016), and Dong. (2017); for the illite Rb–Sr ages are from Jin. (2017); for the calcite Sm–Nd ages are from Su et al. (2009), Jin. (2017), Tan et al. (2019), and Wang et al. (2021); for the fluid inclusion Rb–Sr ages are from Jin. (2017) and Zheng et al. (2019). In-situ dating results of hydrothermal rutile are from Pi et al. (2017) and Gao et al. (2021); for monazite are from Gao et al. (2021); for hydrothermal apatite are from Chen et al. (2019), Ji et al. (2023), Lin et al. (2023), and Gao et al. (2023a); for calcite are from Jin et al. (2021).

mineralization in the basin, at ca. 230–200 Ma and 160–130 Ma, respectively (Hu et al., 2017; Su et al., 2018). However, whether the latter represents a discrete Carlin-type gold mineralization event has been questioned. Some scholars proposed that only the sulfide Re–Os ages of 230–200 Ma can record the primary timing of gold mineralization, given that pyrite and arsenopyrite are the most important gold-bearing sulfides. In contrast, the Sm–Nd ages (160–130 Ma) of calcite, the most important gangue minerals, were interpreted to represent the timing of a post-ore hydrothermal fluid superposition event related to late-stage Sb-Hg mineralization (Li et al., 2022b; Hu et al., 2022). Unequivocal textural relationships with gold-bearing pyrite and mature dating methods are two prerequisites for taking mineral ages as the timing of gold mineralization. However, the pyrite and arsenopyrite in Carlin-type gold deposits are commonly characterized by complex core–rim zoning with sharp contacts and disparate elemental and isotopic compositions, which indicate that core and rim formed in discrete hydrothermal events (Barker et al., 2009; Su et al., 2012; Xie et al., 2018; Gao et al., 2022). Additionally, these two ore minerals generally contain organic matter inclusions (Chen et al., 2015), which commonly have much higher Re and Os concentrations than the sulfide host and, therefore, strongly influence the dating of sulfides (Huang et al., 2022). Similarly, the sericite or illite in Carlin-type gold deposits is commonly too fine-grained to be mechanically separated from the inheritances of pre-ore mineral (Hofstra et al., 1999; Arehart et al., 2003). For calcite, it is difficult to identify which calcite is ore stage (Xie et al., 2018), and individual calcite vein may have precipitated from several discrete fluid episodes with significant time gap at the microscale (Jin et al., 2021; Ge et al., 2022). Therefore, the inherent problems of these dissolution-based bulk analyses on mineral separates make their ages highly questionable, as pointed out by Xie et al. (2018).

In contrast, *in-situ* dating techniques can precisely target the mineral or growth zone that shows intimate textural associations with gold-bearing pyrite and, therefore, provide more robust age constraints on the timing of gold mineralization. We compiled recently reported *in-situ* dating results for hydrothermal rutile, monazite, apatite, and calcite from the Youjiang Carlin-type gold deposits. As exhibited in Fig. 8**b**, these age data concentrate in two peaks of ca. 215–200 Ma and 155–140 Ma, respectively. These new data strongly suggest an episode of Carlin-type gold mineralization during the Late Triassic in the Youjiang basin, as represented by the Zhesang deposit (Pi et al., 2017). However, they also raise the possibility that the latter records only a post-ore hydrothermal superposition event that disturbed or reset the primary chronometers. *In-situ* U–Pb dating on hydrothermal calcite from the Shuiyindong deposit in the basin revealed simultaneously these two hydrothermal fluid infiltration events (Jin et al., 2021), indicating that multiple hydrothermal fluid episodes affected the Carlin-type gold deposits in the Youjiang basin.

Cherniak. (2010) and Millonig et al. (2013) have determined the relative retentivity of Pb during hydrothermal modification of accessory minerals and revealed that the hydrothermal zircon U–Th–Pb chronometer is much more resistant to modification than that of apatite, titanite, zirconolite, monazite, or pyrochlore. Zhao et al. (2017) and Li et al. (2018, 2021a) have also suggested that the hydrothermal zircon U–Pb system can heartly survive multiple hydrothermal events in geologically complex deposits, and that it is a very robust chronometer for recording primary mineralization ages, even if the host rocks have experienced intensive modification. The integrated petrographic, textural, and compositional features suggest that the zircon grains with

ages of ca. 140 Ma from the mineralized dolerite of Badu are of hydrothermal and crystallized from the hydrothermal fluids during the pyrite–sericite–carbonate–quartz alterations associated with gold mineralization. Thus, this age robustly represents the primary timing of the Badu Carlin-type gold mineralization, suggesting existence of a true episode of Carlin-type gold mineralization during the Early Cretaceous in the Youjiang basin.

This age is within errors compatible with the recently acquired independent dating constraints on hydrothermal rutile (141.8 ± 5.7 Ma) and monazite (143.5 ± 1.4 Ma) at the Badu deposit (Gao et al., 2021) and those of hydrothermal apatite at the Shuiyindong, Zimudang, Jinfeng, Jinya, Linwang, Nibao, Mingshan, and Gaolong deposits in the basin (ca. 150–140 Ma, Chen et al., 2019; Ji et al., 2023; Lin et al., 2023; Gao et al., 2023a). Given that the hydrothermal zircon is a very robust chronometer recording the primary formation age, the highly consistent ages indicate that these mineral chronometers are unlikely to have formed during the Late Triassic and then been disturbed or reset during the Early Cretaceous. In that case, the hydrothermal zircon would have a U–Pb age of ca. 210 Ma, and the other minerals would yield a series of younger ages mixing between ca. 210 Ma and ca. 140 Ma, as is the case in the Bayan Obo REE deposit (Li et al., 2021a, 2021b). However, this does not accord with the true dating results. Additionally, the highly consistent ages (Fig. 9) suggest that the other three minerals with different retentivities of Pb can represent the mineralization ages of the Carlin-type gold deposits in the Youjiang basin. The similarity of the geological and mineralization features of these deposits also suggests that they probably formed during a single metallogenic event (Gao et al., 2021). In summary, the geochronological data presented in this study, in combination with previous results, suggest a pervasive Early Cretaceous Carlin-type gold mineralization event in the Youjiang basin.

6.3. *Implications for the dynamic setting and genesis of the Youjiang Carlin-type gold deposits*

The new mineralization ages in this study, together with the recently published *in-situ* dating results for other gold deposits, collectively define two episodes of Carlin-type gold mineralization in the Youjiang basin, i.e., the Late Triassic (215–210 Ma) and Late Jurassic-Early Cretaceous (150–140 Ma). These reliable ages enable us to have a better understanding on the dynamic settings of Carlin-type gold mineralization in the region, which are discussed below.

South China experienced far-reaching Triassic (Indosinian) and Jurassic-Cretaceous (Yanshanian) tectonothermal events during the Mesozoic (Wang et al., 2013; Dong et al., 2015). The Youjiang basin is geographically located at the southwestern margin of South China, and its Triassic evolution was commonly considered to be controlled by closure of the Paleo-Tethys Ocean and subsequent collisions between the South China and Indochina Blocks along the Ailaoshan – Song Ma suture zone to the south (Yan et al., 2006; Cai and Zhang, 2009; Qiu et al., 2016; Yang et al., 2021). The age peak of the collision and related metamorphism is at ca. 246 Ma (Wang et al., 2013). Compression related to the collision was temporally N-ward propagated to the Youjiang basin, forming NNW-trending top-to-the-north Youjiang thrust-fold-systems that involve the Middle Triassic strata (Qiu et al., 2016; Yang et al., 2021). Since ca. 230 Ma, South China has entered into post-collision intracontinental evolution stage (Wang et al., 2013). Therefore, the Late Triassic gold mineralization event in the Youjiang basin, represented by the Zhesang deposit, may be related to a post-collisional setting of Indosinian orogeny.

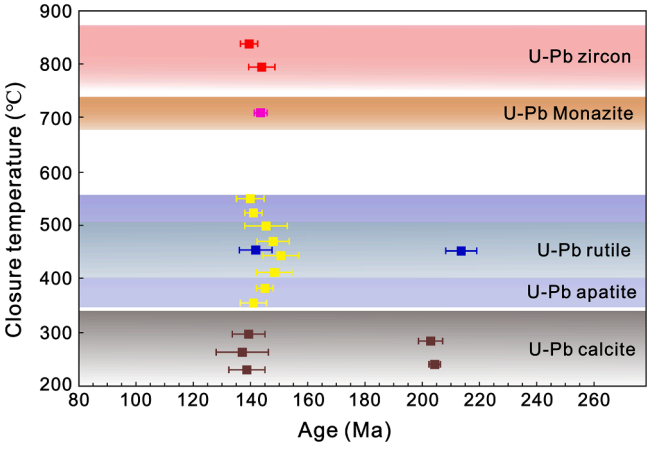

Fig. 9. Summary of *in-situ* U-Pb ages of hydrothermal minerals and their corresponding closure temperatures for the Carlin-type gold deposits in the Youjiang basin. The data sources are same with Fig. 8. Hydrothermal zircon has the highest retentivity of Pb.

Since the Middle Jurassic, the dominant tectonic regime of South China gradually changed from a Tethyan domain to a Pacific domain due to subduction of the Izanagi plate or Paleo-Pacific plate beneath the eastern margin of the Eurasian continent (Mao et al., 2011; Li et al., 2014; Dong et al., 2015). Asthenosphere upwelling and large-scale lithospheric extension were assumed to occur in the interior of South China during the Late Jurassic to Early Cretaceous, which triggered extensive granitic magmatism and its related W-Sn metallogenesis with ages of 160–140 Ma (Hu and Zhou, 2012; Mao et al., 2013, 2020). The second episode of Calin-type gold mineralization in the Youjiang basin, represented by the Shuiyindong, Jinfeng, Linwang, Jinya, and Badu deposits, coincide in time with such large-scale metallogenesis of South China. Additionally, some igneous rocks with ages of 160–136 Ma, which were also formed under extensional setting, occur within and around the basin (Li et al., 2013a; Gan et al., 2020; Su et al., 2021b). Taken together, the Late Jurassic-Early Cretaceous Carlin-type gold mineralization in the Youjiang basin may be associated with large-scale lithospheric extension of South China, interpreted as a far-field response to the subduction and rollback of the Paleo-Pacific plate (Hu et al., 2017; Gao et al., 2021, 2023a).

Carlin-type gold deposits in the Youjiang basin were sometimes classified as orogenic gold deposit associated with Indosinian orogeny (Goldfarb and Groves, 2015; Goldfarb et al., 2019; Yang et al., 2020). This interpretation was largely based on the occurrence of these deposits (e.g., Jinfeng and Jinya) within the compressional structures, e.g., tight anticline, thrust, and/or shear zone (Yang et al., 2020). However, several lines of evidence argue against their classification as orogenic gold deposits: (1) Orogenic gold deposits are commonly considered to occur within metamorphic terranes and form at compressional to transpression stage of orogeny (Goldfarb et al., 2001, 2005; Goldfarb and Groves, 2015). However, precise mineralization ages suggest that low-temperature gold deposits in the Youjiang basin, especially for those with the Late Jurassic-Early Cretaceous ages, significantly postdates (nearly one hundred m.y. younger) the Indosinian orogeny and formed in extensional setting. Additionally, no orogeny-related regional metamorphism has been documented in the basin (Suo et al., 1998); (2) Published $\delta^{34}S$ values of gold-bearing pyrite, together with noble gas, Hg, and Mg isotopic data, suggest that the reduced sulfur and ore metals in the initial auriferous fluids were sourced from deep reservoirs rather sedimentary strata surrounding gold mineralization (Yan et al., 2018; Xie et al., 2018, 2022; Jin et al., 2020; Gao et al., 2022, 2023b). This contrasts with the genetic model of metamorphic devolatilization of supracrustal rock for orogenic gold deposit (Goldfarb et al., 2001, 2005; Goldfarb and Groves, 2015); (3) The geological features of the gold deposits in the Youjiang basin, including hydrothermal alteration, mineral paragenesis, gold occurrence, and formation condition, are identical to typical Carlin-type gold deposits in Nevada. In view of these facts, we therefore proposed that low-temperature gold deposits in the Youjiang basin, at least most of them, are of equivalents of Carlin-type gold deposit.

6.4. Hydrothermal zircon as a potential clock for magmatic rock-hosted Carlin-type gold deposits

Constraining the timing of Carlin-type gold deposits is particularly difficult, partly due to the lack of minerals that are clearly related to gold mineralization and are amenable to radiometric dating (Hu et al., 2002, 2017; Arehart et al., 2003). Although most of Carlin-type gold deposits are hosted by carbonaceous sedimentary rocks, some deposits in Nevada and the Youjiang basin occur within igneous rock (Ressel et al., 2000; Yigit and Hofstra, 2003; Pi et al., 2017; Su et al., 2018; Gao et al., 2021). These deposits provide unique opportunities to date Carlin-type gold mineralization, because their host rocks are largely free from the earlier diagenetic and thermal effects experienced by sedimentary strata, and the magmatic zircon in the igneous host can place a maximum timing constraint on gold mineralization. Importantly, our study shows that hydrothermal zircon can form from low-temperature hydrothermal fluids of Carlin-type gold mineralization. When confidently identified by integrating textural and compositional data and comparing these with those of associated magmatic zircon, hydrothermal zircon can be used to provide robust constraints on the timing of primary Carlin-type gold mineralization, because of its high retentivity of Pb and ability to survive hydrothermal events.

7. Conclusions

Hydrothermal zircon grains coeval with gold mineralization were identified in mineralized dolerite from the Badu dolerite-hosted Carlin-type gold deposit in the Youjiang basin of South China. In-situ SIMS and LA-ICP-MS U-Pb dating on these zircons suggests that the Badu formed at ca. ~ 140, strongly confirming an episode of Carlin-type gold mineralization during the Early Cretaceous in the Youjiang basin, which may be driven by the lithospheric extension of South China related to subduction and rollback of the Paleo-Pacific plate. Our case demonstrates that hydrothermal zircon is a robust chronometer for magmatic rock-hosted Carlin-type gold deposits.

Declaration of Competing Interest

The authors declare that they have no known competing financial interests or personal relationships that could have appeared to influence the work reported in this paper.

Data availability

Data will be made available on request.

Acknowledgements

This work is supported by the National Key R&D Program (2018YFA0702605) and National Natural Science Foundation of China (42103067, 41830432, U1812402). We are grateful to Mr. Yu Liu, Ms. Xiaoxiao Ling, and Ms. Jiao Li for helping with SIMS zircon U-Th-Pb isotope analyses.

Appendix A. Supplementary data

Supplementary data to this article can be found online at https://doi.org/10.1016/j.oregeorev.2023.105771.

References

Arehart, G.B., Chakurian, A.M., Tretbar, D.R., Christensen, J.N., McInnes, B.R., Donelick, R.A., 2003. Evaluation of radioisotope dating of Carlin-type deposits in the Great Basin, western North America, and implications for deposit genesis. Econ. Geol. 98, 235–248.

Ayers, J.C., Peters, T.J., 2018. Zircon/fluid trace element partition coefficients measured by recrystallization of Mud Tank zircon at 1.5 GPa and 800–1000°C. Geochim. Cosmochim. Acta 223, 60–74.

Bao, Z.W., Sun, W.D., Li, C.J., Zhao, Z.H., 2014. U-Pb dating of hydrothermal zircon from the Dongping gold deposit in North China: Constraints on the mineralization processes. Ore Geol. Rev. 61, 107–119.

Barker, S.L., Hickey, K.A., Cline, J.S., Dipple, G.M., Kilburn, M.R., Vaughan, J.R., Longo, A.A., 2009. Uncloaking invisible gold: use of NanoSIMS to evaluate gold, trace elements, and sulfur isotopes in pyrite from Carlin-type gold deposits. Econ. Geol. 104, 897–904.

Cai, J.X., Zhang, K.J., 2009. A new model for the Indochina and South China collision during the Late Permian to the Middle Triassic. Tectonophysics 467, 35–43.

Chen, M.H., Huang, Q.W., Hu, Y.Z., Chen, Z.Y., Zhang, W., 2009. Genetic types of phyllosilicate (mica) and its 39Ar/40Ar dating in Lannigou gold deposit. Guizhou Province. China. Acta Mineral Sin. 29, 353–362 in Chinese with English abstract.

Chen, M.H., Mao, J.W., Li, C., Zhang, Z.Q., Dang, Y., 2015. Re-Os isochron ages for arsenopyrite from Carlin-like gold deposits in the Yunnan-Guizhou-Guangxi "golden triangle", southwestern China. Ore Geol. Rev. 64, 316–327.

Chen, M.H., Bagas, L., Liao, X., Zhang, Z.Q., Li, Q.L., 2019. Hydrothermal apatite SIMS Th-Pb dating: Constraints on the timing of low-temperature hydrothermal Au deposits in Nibao, SW China. Lithos 324–325, 418–428.

Chen, R.X., Zheng, Y.F., Xie, L.W., 2010. Metamorphic growth and recrystallization of zircon: distinction by simultaneous in-situ analyses of trace elements, U-Th-Pb and Lu-Hf isotopes in zircons from eclogite-facies rocks in the Sulu orogen. Lithos 114, 132–154.

Chen, Y.X., Zheng, Y.F., Chen, R.X., Zhang, S.B., Li, Q.L., Dai, M.N., Chen, L., 2011. Metamorphic growth and recrystallization of zircons in extremely 18O-depleted rocks during eclogite-facies metamorphism: Evidence from U-Pb ages, trace elements, and O-Hf isotopes. Geochim. Cosmochim. Acta 75, 4877–4898.

Cherniak, D.J., 2010. Diffusion in accessory minerals: Zircon, titanite, apatite, monazite and xenotime. Rev. Mineral. Geochem. 72, 827–869.

Cherniak, D.J., Watson, E.B., 2003. Diffusion in zircon. Rev. Mineral. Geochem. 53, 113–143.

Chiaradia, M., Schaltegger, U., Spikings, R.A., Wotzlaw, J.F., Ovtcharova, M., 2013. How accurately can we date the duration of magmatic-hydrothermal events in porphyry systems? -an invited paper. Econ. Geol. 108, 565–584.

Chiaradia, M., Schaltegger, U., Spikings, R.A., 2014. Time scales of mineral systems-advances in understanding over the past decade. Econ. Geol. 18, 37–58.

Claoue-Long, J.C., King, R.W., Kerrich, R., 1990. Archean hydrothermal zircon in the Abitibi Greenstone Belt: constraints on the timing of gold mineralization. Earth Planet. Sci. Lett. 98, 109–128.

Corfu, F., Hanchar, J.M., Hoskin, P.W.O., Kinny, P., 2003. Atlas of zircon textures. Rev. Mineral. Geochem. 53, 469–500.

Deng, X.D., Li, J.W., Wen, G., 2015. U-Pb geochronology of hydrothermal zircons from the early Cretaceous iron skarn deposits in the Handan-Xingtai district, North China Craton. Econ. Geol. 110, 2159–2180.

Dong, S.W., Zhang, Y.Q., Zhang, F.Q., Cui, J.J., Chen, X.H., Zhang, S.H., Miao, L.C., Li, J. H., Shi, W., Li, Z.H., Huang, S.Q., Li, H.L., 2015. Late Jurassic-Early Cretaceous continental convergence and intracontinental orogenesis in East Asia: A synthesis of the Yanshan Revolution. J. Asian Earth Sci. 114, 750–770.

Dong, W.D., 2017. Geochemistry of dolerite-hosted gold deposit along the southern margin of Youjiang basin. Unpublished Ph.D. dissertation, Guiyang, China, Institute of Geochemistry, Chinese Academy of Sciences (in Chinese with English abstract).

Du, Y.S., Huang, H.W., Huang, Z.Q., Xu, Y.J., Yang, J.H., Huang, H., 2009. Basin translation from Late Paleozoic to Triassic of Youjiang basin and its tectonic signification. Geo. Sci. Tech. Info. 28, p. 10–15 (in Chinese with English abstract).

Du, Y.S., Huang, H., Yang, J.H., Huang, H.W., Tao, P., Huang, Z.Q., Hu, L.S., Xie, C.X., 2013. The basin translation from Late Paleozoic to Triassic of the Youjiang basin and its tectonic signification. Geo. Rev. 59, 1–11 in Chinese with English abstract.

Fan, W.M., Zhang, C.H., Wang, Y.J., Guo, F., Peng, T.P., 2008. Geochronology and geochemistry of Permian basalts in western Guangxi Province, Southwest China: Evidence for plume-lithosphere interaction. Lithos 102, 218–236.

Gan, C.S., Wang, Y.J., Barry, T.L., Zhang, Y.Z., Qian, X., 2020. Late Jurassic high-Mg andesites in the Youjiang Basin and their significance for the southward continuation of the Jiangnan Orogen. South China. Gondwana Res. 77, 260–273.

Gao, W., Hu, R.Z., Huang, Y., Zhu, J.J., Li, Q.L., Mei, L., Bi, X.W., Liu, J.Z., 2023a. Hydrothermal apatite as a robust U-Th-Pb chronometer for the Carlin-type gold deposits in the Youjiang basin, SW China. Miner. Deposita https://doi.org/10.1007/s00126-023-01196-6.

Gao, W., Hu, R.Z., Wang, X.Y., Yin, R.S., Bi, X.W., Xie, Z.J., Fu, S.L., Yan, J., 2023b. Large-scale basement mobilization endows the giant Carlin-type gold mineralization in the Youjiang Basin, South China: Insights from mercury isotopes. Geol. Sco. Am. Bull. https://doi.org/10.1130/B36636.1.

Gao, W., Hu, R.Z., Hofstra, A.H., Li, Q.L., Zhu, J.J., Peng, K.Q., Mu, L., Huang, Y., Ma, J. W., Zhao, Q., 2021. U-Pb Dating on Hydrothermal Rutile and Monazite from the Badu Gold Deposit Supports an Early Cretaceous Age for Carlin-Type Gold Mineralization in the Youjiang Basin, Southwestern China. Econ. Geol. 116, 1355–1385.

Gao, W., Hu, R.Z., Mei, L., Bi, X.W., Fu, S.L., Huang, M.L., Yan, J., Li, J.W., 2022. Monitoring the evolution of sulfur isotope and metal concentrations across gold-bearing pyrite of Carlin-type gold deposits in the Youjiang Basin. SW China. Ore Geol. Rev. 147, 104990.

Ge, X., Selby, D., Liu, J.J., Chen, Y.Z., Cheng, G.F., Shen, C.B., 2021. Genetic relationship between hydrocarbon system evolution and Carlin-type gold mineralization: Insights from Re-Os pyrobitumen and pyrite geochronology in the Nanpanjiang Basin. South China. Chem. Geol. 559, 119953.

Ge, X., Shen, C.B., Zhou, R.J., He, P., Zhao, J.X., Feng, Y.X., 2022. Tracing fluid evolution in sedimentary basins with calcite geochemical, isotopic and U-Pb geochronological data: Implications for petroleum and mineral resource accumulation in the Nanpanjiang Basin, South China. Geol. Sco. Am. Bull. 134, 2097–2114.
Goldfarb, R., Baker, T., Dube, B., Groves, D.I., Hart, C.J., Gosselin, P., 2005. Distribution, character and genesis of gold deposits in metamorphic terranes. Econ. Geol. 100th Anniversary Volume, 407–450.
Goldfarb, R.J., Groves, D.I., Gardoll, S., 2001. Orogenic gold and geologic time: A global synthesis. Ore Geol. Rev. 18, 1–75.
Goldfarb, R.J., Groves, D.I., 2015. Orogenic gold: Common or evolving fluid and metal sources through time. Lithos 233, 2–26.
Goldfarb, R., Qiu, K.F., Deng, J., Chen, Y.J., Yang, L.Q., 2019. Orogenic gold deposits of China: Society of Economic Geologists, Inc. Econ. Geol. 22, 263–324.
Hofstra, A.H., Snee, L.W., Rye, R.O., Folger, H.W., Phinisey, J.D., Loranger, R.J., Dahl, A. R., Naeser, C.W., Stein, H.J., Lewchuk, M., 1999. Age constraints on Jerritt Canyon and other Carlin-type gold deposits in the western United States-relationship to Mid-Tertiary extension and magmatism. Econ. Geol. 94, 769–802.
Hoskin, P.W.O., 2005. Trace-element composition of hydrothermal zircon and the alteration of Hadean zircon from the Jack Hills. Australia. Geochim. Cosmochim. Acta 69, 637–648.
Hu, R.G., Pang, B.C., Bai, X.J., Brouwer, F.M., Bai, L.A., Liu, X.J., Li, Y.Q., Xu, J.Q., Qiu, H.N., 2022. Progressive crushing 40Ar/39Ar dating of a gold-bearing quartz vein from the Liaotun Carlin-type gold deposit, Guangxi, southern China. Sci. Rep. 12, 12793.
Hu, R.Z., Su, W.C., Bi, X.W., Tu, G.Z., Hofstra, A.H., 2002. Geology and geochemistry of Carlin-type gold deposits in China. Miner. Deposita 37, 378–392.
Hu, R.Z., Fu, S.L., Huang, Y., Zhou, M.F., Fu, S.H., Zhao, C.H., Wang, Y.J., Bi, X.W., Xiao, J.F., 2017. The giant South China Mesozoic low-temperature metallogenic domain, Reviews and a new geodynamic model. J. Asian Earth Sci. 137, 9–34.
Hu, R.Z., Wen, H.J., Ye, L., Chen, W.T., Xia, Y., Fan, H.F., Huang, Y., Zhu, J.J., Fu, S.L., 2020. Metallogeny of critical metals in the Southwestern Yangtze Block. Chin. Sci. Bull. 65, 3700–3714 in Chinese with English abstract.
Hu, R.Z., Zhou, M.F., 2012. Multiple Mesozoic mineralization events in South China-an introduction to the thematic issue. Miner. Deposita 47, 579–588.
Huang, S.Q., Song, Y.C., Zhou, L.M., Leach, D.L., Chang, Z.S., Hou, Z.Q., 2022. Influence of organic matter on Re-Os dating of sulfides: insight from the giant Jinding sedimentary-hosted Zn-Pb deposit. China. Econ. Geol. 117, 737–745.
Ji, X.Z., Chen, M.H., Yang, L.Q., Chen, G., 2023. The relationship between Carlin-type Au mineralization and magmatism in the Youjiang Basin-a case study from the Mingshan gold deposit in northwest Guangxi. China. Ore Geol. Rev. 157, 105400.
Jiang, W., Xiang, Z.J., Xia, W.J., Xia, L., Zhang, H., Phan, V.T., Yan, Q.R., Wei, W., 2017. Are the mafic intrusive rocks in the Funing area, southeast Yunnan (Southwest China), really derived from the Emeishan plume: New evidence from geological surveys of the Dongbo and Guichao sheets (1:50,000). Acta Petrol. Sin. 33, 3109–3122 in Chinese with English abstract.
Jin, X.Y., 2017. Geology, mineralization and genesis of the Nibao, Shuiyindong and Yata gold deposit in SW Guizhou province, China. University of Geosciences (in Chinese with English abstract), Wuhan, China, China. Ph.D. dissertation.
Jin, X.Y., Hofstra, A.H., Hunt, A.G., Liu, J.Z., Yang, W., Li, J.W., 2020. Noble gases fingerprint the source and evolution of ore-forming fluids of Carlin-type gold deposits in the golden triangle, South China. Econ. Geol. 115, 455–469.
Jin, X.Y., Zhao, J.X., Feng, Y.X., Hofstra, A.H., Deng, X.D., Zhao, X.F., Li, J.W., 2021. Calcite U-Pb dating unravels the age and hydrothermal history of the giant Shuiyindong Carlin-type gold deposits in the golden triangle, South China. Econ. Geol. 116, 1253–1265.
Käpyaho, A., Molnár, F., Sorjonen-Ward, P., Mänttäri, I., Sakellaris, G., Whitehouse, M.J., 2017. New U-Pb age constraints for the timing of gold mineralization at the Pampalo gold deposit, Archaean Hattu schist belt, eastern Finland, obtained from hydrothermally altered and recrystallised zircon. Precambr. Res. 289, 48–61.
Kerrich, R., King, R., 1993. Hydrothermal zircon and baddeleyite in Val d'Or Archean mesothermal gold deposits: characteristics, compositions and fluid-inclusion properties, with implications for timing of primary gold mineralization. Can. J. Earth Sci. 30, 2334–2352.
Kooijman, E., Upadhyay, D., Mezger, K., Raith, M.M., Berndt, J., Srikantappa, C., 2011. Response of the U-Pb chronometer and trace elements in zircon to ultrahigh-temperature metamorphism: the Kadavur anorthosite complex, southern India. Chem. Geol. 290, 177–188.
Lamarao, C.N., Marques, G.T., de Oliveira, D.C., Costi, H.T., Borges, R.M.K., Dall'Agnol, R., 2018. Morphology and composition of zircons in rare metal granites from Brazilian tin provinces. J. South Am. Earth Sci. 84, 1–15.
Lawrie, K., Mernagh, T.P., Ryan, C.G., van Achterbergh, E., Black, L.P., 2007. Chemical fingerprinting of hydrothermal zircons: an example from the Gidginbung high sulphidation Au-Ag-(Cu) deposit, New South Wales. Australia. Proc. Geol. Assoc. 118, 37–46.
Lee, J.K., Williams, I.S., Ellis, D.J., 1997. Pb, U and Th diffusion in natural zircon. Nature 390, 159–162.
Li, X.C., Fan, H.R., Zeng, X., Yang, K.F., Yang, Z.F., Wang, Q.W., Li, H.T., 2021b. Identification of ~1.3 Ga hydrothermal zircon from the giant Bayan Obo REE deposit (China): Implication for dating geologically-complicated REE ore system. Ore Geol. Rev. 138, 104405.
Li, P.Y., Guan, S.J., Hu, Y.Z., Tian, Z.D., Cheng, Y., Wang, X.L., Tan, X.L., Zhou, L., 2022a. Origin and Re-Os geochronology of vein bitumen in the Nanpanjiang basin, SW China: Implication for the ore-forming age of Carlin-type gold deposits. Ore Geol. Rev. 1497, 105118.
Li, Z.X., Li, X.H., 2007. Formation of the 1300-km-wide intracontinental orogen and postorogenic magmatic province in Mesozoic South China: A flat-slab subduction model. Geology 35, 179–182.
Li, Q.L., Li, X.H., Liu, Y., Tang, G.Q., Yang, J.H., Zhu, W.G., 2010. Precise U-Pb and Pb-Pb dating of Phanerozoic baddeleyite by SIMS with oxygen flooding technique. Jour. Analy. Atom. Spec. 25, 1107–1113.
Li, Q.L., Li, X.H., Wu, F.Y., Yin, Q.Z., Ye, H.M., Liu, Y., Tang, G.Q., Zhang, C.L., 2012. In-situ SIMS U-Pb dating of phanerozoic apatite with low U and high common Pb. Gondwana Res. 21, 745–756.
Li, C., Li, L., Li, S.R., Santosh, M., Shen, J.F., 2022b. Geochemistry of hydrothermal zircon as a proxy to fingerprint ore fluids in late Mesozoic decratonic gold deposits. Ore Geol. Rev. 143, 104703.
Li, X.H., Liu, Y., Li, Q.L., Guo, C.H., Chamberlain, K.R., 2009. Precise determination of Phanerozoic zircon Pb/Pb age by multi-collector SIMS without external standardization. Geochem. Geophys. Geosyst. 10, Q04010.
Li, Y., Selby, D., Condon, D., Tapster, S., 2017. Cyclic magmatic-hydrothermal evolution in porphyry systems: High-precision U-Pb and Re-Os geochronology constraints on the Tibetan Qulong porphyry Cu-Mo deposit. Econ. Geol. 112, 1419–1440.
Li, Y., Li, X.H., Selby, D., Li, J.W., 2018b. Pulsed magmatic fluid release for the formation of porphyry deposits: Tracing fluid evolution in absolute time from the Tibetan Qulong Cu-Mo deposit. Geology 46, 7–10.
Li, X.H., Tang, G.Q., Gong, B., Yang, Y.H., Hou, K.J., Hu, Z.C., Li, Q.L., Liu, Y., Li, W.X., 2013b. Qinghu zircon: A working reference for microbeam analysis of U-Pb age and Hf and O isotopes. Chin. Sci. Bull. 58, 4647–4654.
Li, J.K., Wang, D.H., Li, H.Q., Chen, Z.H., Mei, Y.P., 2013a. Late Jurassic-Early Cretaceous mineralization in the Laojunshan ore concentration area. Yunnan Province. Earth Sci. 38, 1023–1036 in Chinese with English abstract.
Li, W., Xie, G.Q., Mao, J.W., Cook, N.J., Wei, H.T., Ji, Y.H., Fu, B., 2023. Precise age constraints for the Woxi Au-Sb-W deposit, South China. Econ. Geol. 118, 509–518.
Li, X.C., Yang, K.F., Spandler, C., Fan, H.R., Zhou, M.F., Hao, J.L., Yang, Y.H., 2021c. The effect of fluid-aided modification on the Sm-Nd and Th-Pb geochronology of monazite and bastnäsite: Implication for resolving complex isotopic age data in REE ore systems. Geochim. Cosmochim. Acta 300, 1–24.
Li, J.H., Zhang, Y.Q., Dong, S.W., Johnston, S.T., 2014. Cretaceous tectonic evolution of South China: A preliminary synthesis. Earth Sci. Rev. 134, 98–136.
Li, J.H., Wu, P., Xie, Z.J., Liu, J.Z., Zhang, S.J., Song, W.F., Zhang, B.Q., Li, S.T., Xu, L.Y., Zheng, L.L., 2021a. Alteration and paragenesis of the basalt-hosted Au deposits, southwestern Guizhou Province, China: Implications for ore genesis and exploration. Ore Geol. Rev. 131, 104034.
Li, X.C., Zhou, M.F., Chen, W.T., Zhao, X.F., Tran, M.D., 2018a. Uranium-lead dating of hydrothermal zircon and monazite from the Sin Quyen Fe-Cu-REE-Au-(U) deposit, northwestern Vietnam. Miner. Deposita 53, 399–416.
Li, L.X., Zi, J.W., Li, H.M., Rasmussen, B., Wilde, S.A., Sheppard, S., Ma, Y.B., Meng, J., Song, Z., 2019. High-grade magnetite mineralization at 1.86 Ga in Neoarchean banded iron formations, Gongchangling, China: in situ U-Pb geochronology of metamorphic-hydrothermal zircon and monazite. Econ. Geol. 114, 1159–1175.
Lin, S.R., Hu, K., Cao, J., Liu, Y., Liu, S.J., Zhang, B., 2023. Geochemistry and origin of hydrothermal apatite in Carlin-type Au deposits, southwestern China (Gaolong deposit). Ore Geol. Rev. 157, 105312.
Liu, S.Q., Chen, M.H., Yang, F., Dai, Y., Zhang, Y., 2014. Re-Os dating and sulfur isotope tracing of arsenopyrites from Jinya gold deposit in Guangxi. Jour. Guilin Uni. Tech. 34, 423–430.
Liu, Y.S., Hu, Z.C., Gao, S., Günther, D., Xu, J., Gao, C.G., Chen, H.H., 2008. In situ analysis of major and trace elements of anhydrous minerals by LA-ICP-MS without applying an internal standard. Chem. Geol. 257, 34–43.
Liu, Y.S., Hu, Z.C., Zong, K.Q., Gao, C.C., Chen, H.H., 2010b. Reappraisement and refinement of zircon U-Pb isotope and trace element analyses by LA-ICP-MS. Chin. Sci. Bull. 55, 1535–1546.
Liu, S., Su, W.C., Hu, R.Z., Feng, C.X., Gao, S., Coulson, I.M., Wang, T., Feng, G.Y., Tao, Y., Xia, Y., 2010a. Geochronological and geochemical constraints on the petrogenesis of alkaline ultramafic dykes from southwest Guizhou Province, SW China. Lithos 114, 253–264.
Ludwig, K.R., 2003. User's Manual for Isoplot 3.00, a geochronological toolkit for Microsoft Excel. Berkeley Geochronological Center Special Publication 4, 25–32.
Mao, J.W., Xie, G.Q., Duan, C., Pirajno, F., Ishiyama, D., Chen, Y.C., 2011. A tectonogenetic model for porphyry-skarn-strata bound Cu-Au-Mo-Fe and magnetite-apatite deposits along the Middle-Lower Yangtze River Valley. Eastern China. Ore Geol. Rev. 43, 294–314.
Mao, J.W., Cheng, Y.B., Chen, M.H., Pirajno, F., 2013. Major types and time-space distribution of Mesozoic ore deposits in South China and their geodynamic settings. Miner. Deposita 48, 267–294.
Mao, J.W., Wu, S.H., Song, S.W., Dai, P., Xie, G.Q., Su, Q.W., Liu, P., Wang, X.G., Yu, Z. X., Chen, X.Y., Tang, W.X., 2020. The world-class Jiangnan tungsten belt: Geological characteristics, metallogeny, and ore deposit model. Chin. Sci. Bull. 65, 3746–3762.
McDonough, W.F., Sun, S.-S., 1995. The composition of the Earth. Chem. Geol. 120, 223–253.
McNaughton, N.J., Mueller, A.G., Groves, D.I., 2005. The age of the giant Golden Mile deposit, Kalgoorlie, Western Australia: Ion-microprobe zircon and monazite U-Pb geochronology of a synmineralization lamprophyre dike. Econ. Geol. 100, 1427–1440.
Millonig, L.J., Gerdes, A., Groat, L.A., 2013. The effect of amphibolite facies metamorphism on the U-Th-Pb geochronology of accessory minerals from meta-carbonatites and associated meta-alkaline rocks. Chem. Geol. 353, 199–209.
Nesbitt, R.W., Pascual, E., Fanning, C.M., Toscano, M., Sáez, R., AlmodóVar, G.R., 1999. U-Pb dating of stockwork zircons from the eastern Iberian Pyrite Belt. J. Geol. Soc. 156, 7–10.

Pelleter, E., Cheilletz, A., Gasquet, D., Mouttaqi, A., Annich, M., El Hakour, A., Deloule, E., Féraud, G., 2007. Hydrothermal zircons: A tool for ion microprobe U-Pb dating of gold mineralization (Tamlalt-Menhouhou gold deposit-Morocco). Chem. Geol. 245, 135–161.

Pettke, T., Audetat, A., Schaltegger, U., Heinrich, C.A., 2005. Magmatic-to-hydrothermal crystallization in the W-Sn mineralized mole granite (NSW, Australia)-part II: evolving zircon and thorite trace element chemistry. Chem. Geol. 220, 191–213.

Pi, Q.H., Hu, R.Z., Bi, X.W., Peng, K.Q., Wu, J.B., Wei, Z.W., Huang, Y., 2016. Geochronology of the Zhesang gold deposit and mafic rock in Funing County of Yunnan Province, with special reference to the dynamic background of Carlin-type gold deposits in the Dian-Qian-Gui region: Acta Petrol. Sin. 32, 3331–3342 in Chinese with English abstract.

Pi, Q.H., Hu, R.Z., Xiong, B., Li, Q.L., Zhong, R.C., 2017. In situ SIMS U-Pb dating of hydrothermal rutile: reliable age for the Zhesang Carlin-type gold deposit in the golden triangle region. SW China. Miner. Deposita 52, 1179–1190.

Qiu, L., Yan, D.P., Tang, S.L., Wang, Q., Yang, W.X., Tang, X.L., Wang, J.B., 2016. Mesozoic geology of southwestern China: Indosinian foreland overthrusting and subsequent deformation. J. Asian Earth Sci. 122, 91–105.

Qiu, L., Yang, W.X., Yan, D.P., Wells, M.L., Qiu, J.T., Gao, T., Dong, J.M., Zhang, L.L., Wang, F.Y., 2018. Geochronology of early Mesozoic diabase units in southwestern China: metallogenic and tectonic implications. Geol. Mag. 156, 1–16.

Ressel, M.W., Noble, D.C., Henry, C.D., Trudel, W.S., 2000. Dike-hosted ores of the Beast deposit and the importance of Eocene magmatism in gold mineralization of the Carlin trend. Nevada. Econ. Geol. 95, 1417–1444.

Schaltegger, U., 2007. Zircon tiny but timely: hydrothermal zircon. Elements 3, 51–79.

Schaltegger, U., Pettke, T., Audétat, A., Reusser, E., Heinrich, C.A., 2005. Magmatic-to hydrothermal crystallization in the W-Sn mineralized Mole Granite (NSW, Australia)-Part I: crystallization of zircon and REE-phosphates over three million years-a geochemical and U-Pb geochronological study. Chem. Geol. 220, 215–235.

Sláma, J., Košler, J., Condon, D.J., Crowley, J.L., Gerdes, A., 2008. Plešovice zircon-A new natural reference material for U-Pb and Hf isotopic microanalysis. Chem. Geol. 249, 1–35.

Stacey, J.S., Kramers, J.D., 1975. Approximation of terrestrial lead isotope evolution by a two-stage model. Earth Planet. Sci. Lett. 26, 207–221.

Stenger, D.P., Kesler, S.E., Peltonen, D.R., Tapper, C.J., 1998. Deposition of gold in Carlin-type deposits; the role of sulfidation and decarbonation at Twin Creeks. Nevada. Econ. Geol. 93, 201–215.

Su, W.C., Hu, R.Z., Xia, B., Xia, Y., Liu, Y.P., 2009. Calcite Sm-Nd isochron age of the Shuiyindong Carlin-type gold deposit. Guizhou. China. Chem Geol. 258, 269–274.

Su, H.M., Jiang, S.Y., Shao, J.B., Zhang, D.Y., Wu, X.K., Huang, X.Q., 2021b. New identification and significance of Early Cretaceous mafic rocks in the interior South China Block. Sci. Rep. 11, 11396.

Su, W.C., Zhang, H.T., Hu, R.Z., Ge, X., Xia, B., Chen, Y.Y., Zhu, C., 2012. Mineralogy and geochemistry of gold-bearing arsenian pyrite from the Shuiyindong Carlin-type gold deposit, Guizhou, China, implications for gold depositional processes. Miner. Deposita 47, 653–662.

Su, W.C., Dong, W.D., Zhang, X.C., Shen, N.P., Hu, R.Z., Hofstra, A.H., Cheng, L.Z., 2018. Carlin-type gold deposits in the Dian-Qian-Gui "Golden Triangle" of Southwest China. Society of Economic Geologists, Inc. Reviews in Economic Geology, Diversity of Carlin-Type Gold Deposits 20, 157–185.

Su, Z.K., Zhao, X.F., Li, X.C., Zhou, M.F., Kennedy, A.K., Zi, J.W., Spandler, C., Yang, Y. H., 2021a. Unraveling mineralization and multistage hydrothermal overprinting histories by integrated in situ U-Pb and Sm-Nd isotopes in a Paleoproterozoic breccia-hosted IOCG deposit. SW China. Econ. Geol. 116 (7), 1687–1710.

Su, Z.K., Zhao, X.F., Wang, Y.C., Zhu, Z.M., Song, W.L., Spandler, C., 2023. Survival of whole-rock Sm-Nd isotope system from REE redistribution and mineral-scale isotopic resetting amid hydrothermal alteration in REE-rich Fe-Cu deposit. Geochim. Cosmochim. Acta 348, 9–26.

Suo, S.T., Bi, X.M., Zhao, W.X., Hou, G.J., 1998. Very low-grade metamorphism and its geodynamical significance of Triassic strata within the Youjiang River basin. Sci. Geol. Sin. 33, 396–405 in Chinese with English abstract.

Tan, Q.P., Xia, Y., Xie, Z.J., Wang, Z.P., Wei, D.T., Zhao, Y.M., Yan, J., Li, S.T., 2019. Two hydrothermal events at the Shuiyindong Carlin-type gold deposit in southwestern China: Insight from Sm-Nd dating of fluorite and calcite. Minerals 9, 230.

Tera, F., Wasserburg, G.J., 1972. U-Th-Pb systematics in three Apollo 14 basalts and the problem of initial Pb in lunar rocks. Earth Planet. Sci. Lett. 14, 281–304.

Toscano, M., Pascual, E., Nesbitt, R., Almodóvar, G., Sáez, R., Donaire, T., 2014. Geochemical discrimination of hydrothermal and igneous zircon in the Iberian Pyrite Belt. Spain. Ore Geol. Rev. 56, 301–311.

Valley, P.M., Hanchar, J.M., Whitehouse, M.J., 2009. Direct dating of Fe oxide-(Cu-Au) mineralization by U/Pb zircon geochronology. Geology 37, 223–226.

Wang, X., Chen, J., Ren, M.H., 2016. Hydrothermal zircon geochronology: Age constraint on Nanling Range tungsten mineralization (Southeast China). Ore Geol. Rev. 74, 63–75.

Wang, Y., Du, W., Wang, Y.Y., Lin, R.Q., Zhang, D.Q., Zhao, F.P., Sun, Z., Chen, Y., Wang, Y., 2022. Meso-cenozoic tectonic evolution of the ziyun-luodian fault in SW China. Front. Earth Sci. 10, 970944.

Wang, Y.J., Fan, W.M., Zhang, G.W., Zhang, Y.H., 2013. Phanerozoic tectonics of the South China Block: key observations and controversies. Gond. Res. 23, 1273–1305.

Wang, Q.F., Groves, D., 2018. Carlin-style gold deposits, Youjiang basin, China: Tectono-thermal and structural analogues of the Carlin-type gold deposits, Nevada, USA. Miner. Deposita 53, 909–918.

Wang, Z.P., Tan, Q.P., Xia, Y., Liu, J.Z., Yang, C.F., Li, S.T., Li, J.H., Chen, F.E., Wang, X. Y., Pan, Q.Q., Wang, D.F., 2021. Sm-Nd Isochron Age Constraints of Au and Sb Mineralization in Southwestern Guizhou Province. China. Minerals 11, 100.

Wang, R.X., Wang, Q.F., Zhao, J.X., Groves, D.I., Kirkland, C.L., Feng, Y.X., Uysal, I.T., Yang, L., Deng, J., 2023. Carbonate U-Pb and illite Rb-Sr geochronology of sediment-hosted gold: A case study of Yata gold deposit. Chem. Geol. 621, 121352.

Wei, D.T., Zhou, T.F., Xia, Y., Fan, Y., Xie, Z.J., Liu, X.J., Tan, Q.P., Bai, L.A., Wang, F.Y., 2022. Pyrite textural, trace elemental and sulfur isotope signatures of the Badu gold deposit, Youjiang basin (SW China): Implications for ore-fluid source and Au precipitation mechanism. Ore Geol. Rev. 149, 105083.

Wiedenbeck, M., Alle, P., Corfu, F., Griffin, W.L., Meier, M., Oberli, F., Vonquadt, A., Roddick, J.C., Speigel, W., 1995. Three natural zircon standards for U-Th-Pb, Lu-Hf, trace-element and REE analyses. Geostandards Newsletter 19 (1), 1–23.

Williams, I.S., 1998. U-Th-Pb geochronology by ion microprobe. In: McKibben, M.A., Shanks III, W.C., 101 Ridley, W.I. (Eds.), Applications of microanalytical techniques to understanding mineralizing 102 processes. Rev. Econ. Geol. 7, 1–35.

Xia, W.J., Yan, Q.R., Xiang, Z.J., Xia, L., Jiang, W., Li, X.J., Zhou, B., Deng, L., 2019. Baddeleyite and zircon U-Pb dating of Badu diabase in the Nanpanjiang basin and its tectonic significance. Acta Geosci. Sin. 40, 265–278.

Xie, Z.J., Xia, Y., Cline, J.S., Koenig, A., Wei, D.T., Tan, Q.P., Wang, Z.P., 2018. Are there Carlin-type gold deposits in China? A comparison of the Guizhou, China, deposits with Nevada, USA, deposits. Society of Economic Geologists, Inc. Reviews in Economic Geology, Diversity of Carlin-Type Gold Deposits 20, 187–233.

Xie, Z.J., Huang, K.J., Xia, Y., Cline, J., Tan, Q.P., Liu, J.Z., Xiao, J.D., Yan, B., 2022. Heavy δ^{26}Mg values in carbonate indicate a magmatic-hydrothermal origin of Carlin-type Au deposit. Geochim. Cosmochim. Acta 333, 166183.

Yan, J., Hu, R.Z., Liu, S., Lin, Y.T., Zhang, J.C., Fu, S.L., 2018. Nano-SIMS element mapping and sulfur isotope analysis of Au-bearing pyrite from Lannigou Carlin-type Au deposit in SW China: New insights into the origin and evolution of Au-bearing fluids. Ore Geol. Rev. 92, 29–41.

Yan, D.P., Zhou, M.F., Wang, Y.C., Xia, B., 2006. Structural and geochronological constraints on the tectonic evolution of the Dulong-Song Chay tectonic dome in Yunnan province. SW China. J. Asian Earth Sci. 28, 332–353.

Yang, J.H., Cawood, P.A., Du, Y.S., Huang, H., Hu, L.S., 2012. Detrital record of Indosinian mountain building in SW China: Provenance of the Middle Triassic turbidites in the Youjiang Basin. Tectonophysics 574–575, 105–117.

Yang, L., Deng, J., Groves, D.I., Wang, Q.F., Zhang, L., Wu, W., Qin, K., Zhang, Q.Z., 2020. Recognition of two contrasting structural- and mineralogical-gold mineral systems in the Youjiang basin, China-Vietnam: Orogenic gold in the south and Carlin-type in the north. Geosci. Front. 111, 1477–1494.

Yang, W.X., Yan, D.P., Qiu, L., Wells, M.L., Dong, J.M., Gao, T., Zhang, Z., Mu, H.X., Wang, X.W., Wang, F.Y., 2021. Formation and forward propagation of the Indosinian foreland fold-thrust belt and Nanpanjiang foreland basin in SW China. Tectonics 40, e2020TC006552.

Yang, W.B., Niu, H.C., Shan, Q., Sun, W.D., Zhang, H., Li, N.B., Jiang, Y.H., Yu, X.Y., 2014. Geochemistry of magmatic and hydrothermal zircon from the highly evolved Baerzhe alkaline granite: implications for Zr-REE-Nb mineralization. Miner. Deposita 49, 451–470.

Yeats, C.J., McNaughton, N.J., Groves, D.I., 1996. SHRIMP U-Pb geochronological constraints on Archean volcanic-hosted massive sulfide and lode gold mineralization at Mount Gibson, Yilgarn Craton, Western Australia. Econ. Geol. 91, 1354–1371.

Yigit, O., Hofstra, A.H., 2003. Lithogeochemistry of Carlin-type gold mineralization in the Gold Bar district, Battle Mountain-Eureka trend. Nevada. Ore Geol. Rev. 22, 201–224.

Zhao, J.H., Zhou, M.F., Yan, D.P., Zheng, J.P., Li, J.W., 2011. Reappraisal of the ages of Neoproterozoic strata in South China: no connection with the Grenvillian orogeny. Geology 39, 299–302.

Zhao, X.F., Zhou, M.F., Su, Z.K., Li, X.C., Chen, W.T., Li, J.W., 2017. Geology, geochronology, and geochemistry of the Dahongshan Fe-Cu-(Au-Ag) deposit, southwest China: implications for the formation of iron oxide copper-gold deposits in intracratonic rift settings. Econ. Geol. 112, 603–628.

Zheng, L.L., Yang, R.D., Gao, J.B., Chen, J., Liu, J.Z., Li, D.P., 2019. Quartz Rb-Sr isochron ages of two type orebodies from the Nibao Carlin-type gold Deposit, Guizhou, China. Minerals 9, 399–413.

Zhou, Q., Jiang, Y.H., Zhao, P., Liao, S.Y., Jin, G.D., Liu, Z., Jia, R.Y., 2012. SHRIMP U-Pb dating on hydrothermal zircons: evidence for an Early Cretaceous epithermal event in the Middle Jurassic Dexing porphyry copper deposit, Southeast China. Econ. Geol. 107, 1507–1514.

Zhou, M.F., Zhao, J.H., Qi, L., 2006. Zircon U-Pb geochronology and elemental and Sr-Nd isotopic geochemistry of Permian mafic rocks in the Funing area, SW China: Contrib. Mineral. Petrol. 151, 1–19.

Zhu, J.J., Hu, R.Z., Richards, J.P., Bi, X.W., Stern, R., Lu, G., 2017a. No genetic link between Late Cretaceous felsic dikes and Carlin-type Au deposits in the Youjiang basin. Southwest China. Ore Geol. Rev. 84, 328–337.

Zhu, M.T., Zhang, L.C., Dai, Y.P., Wang, C.L., Peng, Z.D., 2017b. Hydrothermal modification of zircon geochemistry and Lu-Hf isotopes from the Hongtoushan Cu–Zn deposit. China. Ore Geol. Rev. 86, 707–718.

Zhuang, X.G., 1995. The paleogeothermal field of northwestern Guangxi: Characteristics and its role in the formation of micro-disseminated gold deposits. Miner. Deposits 14, 82–89 in Chinese with English abstract.